

# Coordinated *Tbx3/Tbx5* transcriptional control of the adult ventricular conduction system

Ozanna Burnicka-Turek<sup>1\*</sup>, Katy A Trampel<sup>2</sup>, Brigitte Laforest<sup>1</sup>, Michael T Broman<sup>3</sup>, Xinan H Yang<sup>1</sup>, Zoheb Khan<sup>1</sup>, Eric Rytkin<sup>2</sup>, Binjie Li<sup>2</sup>, Ella Schaffer<sup>1</sup>, Margaret Gadek<sup>1</sup>, Kaitlyn M Shen<sup>1</sup>, Igor R Efimov<sup>2</sup>, Ivan P Moskowitz<sup>1\*</sup>

<sup>1</sup>Departments of Pediatrics, Pathology, and Human Genetics, University of Chicago, Chicago, United States; <sup>2</sup>Departments of Biomedical Engineering, Northwestern University, Chicago, United States; <sup>3</sup>Department of Medicine, Section of Cardiology, University of Chicago, Chicago, United States

## eLife Assessment

The work presented is **important** for our understanding of the development of the cardiac conduction system and its regulation by T-box transcription factors. The conclusions are supported by **convincing** data. Overall this is an excellent study that advances our understanding of cardiac biology and has implications beyond the immediate field of study.

### \*For correspondence:

burnickatureko@uchicago.edu (OB-T);

imoskowitz@peds.bsd.uchicago.edu (IPM)

**Competing interest:** The authors declare that no competing interests exist.

**Funding:** See page 20

**Sent for Review**

29 August 2024

**Preprint posted**

30 August 2024

**Reviewed preprint posted**

21 November 2024

**Reviewed preprint revised**

17 April 2025

**Version of Record published**

24 July 2025

**Reviewing Editor:** Benoit

Bruneau, University of California, San Francisco, United States

© Copyright Burnicka-Turek

et al. This article is distributed under the terms of the [Creative Commons Attribution License](#), which permits unrestricted use and redistribution provided that the original author and source are credited.

**Abstract** The cardiac conduction system (CCS) orchestrates the electrical impulses that enable coordinated contraction of the cardiac chambers. The T-box transcription factors *TBX3* and *TBX5* are required for CCS development and associated with overlapping and distinct human CCS diseases. We evaluated the coordinated role of *Tbx3* and *Tbx5* in the murine ventricular conduction system (VCS). We engineered a compound *Tbx3:Tbx5* conditional knockout allele for both genes located in cis on mouse chromosome 5. Conditional deletion of both T-box transcriptional factors in the VCS, using the VCS-specific *Mink*<sup>CreERT2</sup>, caused loss of VCS function and molecular identity. Combined *Tbx3* and *Tbx5* deficiency in the adult VCS led to conduction defects, including prolonged PR and QRS intervals and elevated susceptibility to ventricular tachycardia. These electrophysiological defects occurred prior to detectable alterations in cardiac contractility or histologic morphology, indicative of a primary conduction system defect. *Tbx3:Tbx5* double-knockout VCS cardiomyocytes revealed a transcriptional shift toward non-CCS-specialized working myocardium, indicating a change to their cellular identity. Furthermore, optical mapping revealed a loss of VCS-specific conduction system propagation. Collectively, these findings indicate that *Tbx3* and *Tbx5* coordinate to control VCS molecular fate and function, with implications for understanding cardiac conduction disorders in humans.

## Introduction

The cardiac conduction system (CCS) constitutes a highly specialized network of cardiomyocytes that initiate and propagate the electrical impulses required for synchronized contractions of the heart. In the mature mammalian heart, the functional components of the CCS can be broadly divided into the slowly propagating atrial nodes (~5 cm/s), containing the sinoatrial node (SAN) and atrioventricular node (AVN), and the rapidly propagating ventricular conduction system (VCS) (~200 cm/s), including the AV (His) bundle and the right and left bundle branches (BBs). The VCS

is responsible for rapid propagation of the electrical impulse from the AVN to the ventricular apex to enable synchronous ventricular contraction and effective ejection of blood from the ventricles (Arnolds et al., 2012; Park and Fishman, 2011; Moskowitz et al., 2007). Defects of CCS can occur in normally formed hearts as well as in patients with structural congenital heart disease and are a major source of morbidity and mortality (Arnolds et al., 2012; Moskowitz et al., 2007; Munshi, 2012; Rubart and Zipes, 2005; Huikuri et al., 2001). The VCS specifically has been recognized as a substrate for life-threatening ventricular arrhythmias, including bundle branch reentry tachycardia, idiopathic fascicular tachycardia, short-coupled torsade de pointes, and ventricular fibrillation (Arnolds et al., 2012; Huikuri et al., 2001; van Duijvenboden et al., 2014; Arnolds and Moskowitz, 2011b; Scheinman, 2009). Despite the severe clinical consequences of CCS disorders, the molecular mechanisms that establish and maintain regional functionality of the mature CCS domains require further study.

Human genetic studies have identified numerous loci associated with adult human CCS function, including the developmentally important factors *Tbx3* and *Tbx5* (reviewed in Arnolds et al., 2012; Arnolds et al., 2011a). *Tbx3* and *Tbx5* play crucial roles in adult CCS development and function (Arnolds et al., 2012; Moskowitz et al., 2007; Burnicka-Turek et al., 2020; Moskowitz et al., 2004; van Weerd and Christoffels, 2016; van den Boogaard et al., 2012; Bakker et al., 2012; Hatcher and Basson, 2009; Bakker et al., 2008; Hoogaars et al., 2007b; Mori et al., 2006; Bruneau et al., 2001). *Tbx5* encodes a T-box transcriptional activator required for structural and conduction system cardiac development (Moskowitz et al., 2007; Moskowitz et al., 2004; Bruneau et al., 2001; Hoogaars et al., 2007a). Dominant mutations in human *TBX5* cause Holt–Oram syndrome (HOS, OMIM:142900), an autosomal dominant disorder characterized by upper limb malformations, congenital heart defects, and CCS abnormalities (Basson et al., 1997; Li et al., 1997; Basson et al., 1994). The cardiac phenotype of HOS, including atrioventricular conduction delay, has been recapitulated in the *Tbx5* heterozygous mice (Bruneau et al., 2001). Moreover, VCS-specific *Tbx5* knockout caused slowed VCS function and ventricular tachycardia (VT) resulting in sudden death in mice (Arnolds et al., 2012), emphasizing the importance of *Tbx5* in VCS conduction. *Tbx5* is strongly expressed in the atria and VCS (Arnolds et al., 2012; Moskowitz et al., 2007; Moskowitz et al., 2004; Bakker et al., 2008), and directly regulates several targets required for VCS function (Moskowitz et al., 2007; Bruneau et al., 2001; Hiroi et al., 2001), including *Gja5* (*Cx40*) (Bruneau et al., 2001) and *Scn5a* (*Nav1.5*) (Arnolds et al., 2012). *Tbx3* encodes a T-box transcriptional repressor which is critical for cardiac development (Bakker et al., 2008; Frank et al., 2011). Dominant mutations in human *TBX3* cause Ulnar–Mammary syndrome (OMIM:181450), a developmental disorder (Meneghini et al., 2006; Bamshad et al., 1997), that includes functional conduction system defects (Linden et al., 2009). In the heart, *Tbx3* is specifically expressed within CCS (Bakker et al., 2008; Hoogaars et al., 2004), and its deficiency below critical level leads to lethal arrhythmias (Frank et al., 2011). Furthermore, *Tbx3* is required for the molecular identity but not the function of the VCS (Bakker et al., 2008). In contrast, *Tbx3* in SAN and AVN is required for their proper function (Hoogaars et al., 2004), emphasizing its critical role in maintaining proper cardiac rhythm.

A model for regional CCS specialization suggests that the adult CCS is organized entirely as a slow conduction system ground state by *Tbx3* with a T-box-dependent, physiologically dominant fast conduction system network driven specifically in the VCS by *Tbx5* (Burnicka-Turek et al., 2020). The adult VCS-specific removal of *TBX5* or overexpression of *TBX3* shifted the fast VCS into a slow nodal-like system, indicating that the *Tbx3/Tbx5* ratio determines nodal versus VCS function (Burnicka-Turek et al., 2020). However, a comprehensive assessment of the coordinated requirements for *Tbx3* and *Tbx5* has been hindered by the inability to achieve their compound deletion due to their genomic proximity. *Tbx3* and *Tbx5* are situated in cis within 0.6 Mb on chromosome 5 in mice, rendering their simultaneous deletion unattainable with the available single allele conditional alleles. To investigate the consequences of *Tbx3* and *Tbx5* compound removal from the mature VCS, we generated a novel compound *Tbx3:Tbx5* double-conditional allele. We found that VCS-specific genetic removal of both *TBX3* and *TBX5* transformed fast-conducting, adult VCS into working myocardium-like cardiomyocytes, shifting them from conduction to non-conduction myocytes. These results demonstrated the coordinated requirements of both *Tbx3* and *Tbx5* for maintained specification of the mature VCS.

## Results

We generated a novel *Tbx3:Tbx5* double-floxed allele to enable the simultaneous conditional deletion of *Tbx3* and *Tbx5* genes specifically from the adult VCS. *Tbx3* and *Tbx5* reside in cis on mouse chromosome 5 (*Tbx3* mm39 chr5:119808734–119822789; *Tbx5* mm39 chr5:119970733–120023284). Therefore, to generate a double-conditional knockout, we targeted *Tbx5* in the background of a previously validated *Tbx3* floxed allele (Frank et al., 2011) using the CRISPR–Cas9 system (Gurumurthy et al., 2021; Dow et al., 2015; Figure 1A). We engineered a *Tbx5* floxed allele mirroring a previously published allele (Bruneau et al., 2001). This design enabled us to utilize the previously published individual *Tbx3* floxed allele (Frank et al., 2011) and individual *Tbx5* floxed allele (Bruneau et al., 2001) to serve as controls (Figure 1A, Figure 1—figure supplements 1 and 2).

We assessed the impact of removing *Tbx3* and *Tbx5* from the mature VCS by combining the *Tbx3:Tbx5* double-floxed mouse line (*Tbx3<sup>fl/fl</sup>;Tbx5<sup>fl/fl</sup>*) with a VCS-specific, tamoxifen (TM)-inducible Cre transgenic mouse line, *Kcne1<sup>CreERT2</sup>* [Tg(RP23-276l20-*MinK*CreERT2)] – hereafter referred to as *MinK<sup>CreERT2</sup>*, in accordance with existing literature (Figure 1A; Arnolds et al., 2012; Arnolds and Moskowitz, 2011b; Burnicka-Turek et al., 2020). Individual *Tbx3* floxed and *Tbx5* floxed mouse lines combined with *MinK<sup>CreERT2</sup>* transgenic mouse lines (*Tbx3<sup>fl/fl</sup>;Tbx5<sup>+/+</sup>;R26R<sup>eYFP/+</sup>;MinK<sup>CreERT2/+</sup>* and *Tbx3<sup>+/+</sup>;Tbx5<sup>fl/fl</sup>;R26R<sup>eYFP/+</sup>;MinK<sup>CreERT2/+</sup>*, respectively) were generated as controls, and all allelic combinations were evaluated in a mixed genetic background. We compared VCS-specific *Tbx3:Tbx5* double-conditional mutants (*Tbx3<sup>fl/fl</sup>;Tbx5<sup>fl/fl</sup>;R26R<sup>eYFP/+</sup>;MinK<sup>CreERT2/+</sup>*) with control littermates (*Tbx3<sup>+/+</sup>;Tbx5<sup>+/+</sup>;R26R<sup>eYFP/+</sup>;MinK<sup>CreERT2/+</sup>*) and VCS-specific *Tbx3:Tbx5* double-conditional heterozygous littermates (*Tbx3<sup>fl/+</sup>;Tbx5<sup>fl/+</sup>;R26R<sup>eYFP/+</sup>;MinK<sup>CreERT2/+</sup>*). Additionally, we validated the newly created *Tbx5* floxed allele demonstrating that it is efficiently converted to the *Tbx5* null allele through Cre recombinase, causing a phenotype consistent with that observed from conversion of the previously published *Tbx5* floxed allele (Arnolds et al., 2012; Bruneau et al., 2001; Figure 1—figure supplements 1 and 2, Methods section).

We assessed experimental mice at 8–9 weeks of age following tamoxifen administration at 6 weeks of age (Figure 1A, Methods section). We observed loss of both *Tbx3* and *Tbx5* expression, on both the mRNA and protein levels, in the VCS of adult *Tbx3:Tbx5* double-conditional mutant mice (*Tbx3<sup>fl/fl</sup>;Tbx5<sup>fl/fl</sup>;R26R<sup>eYFP/+</sup>;MinK<sup>CreERT2/+</sup>*) but not in their littermate controls (*Tbx3<sup>+/+</sup>;Tbx5<sup>+/+</sup>;R26R<sup>eYFP/+</sup>;MinK<sup>CreERT2/+</sup>*) (Figure 1B, C). Partial loss of *Tbx3* and *Tbx5* expression in the adult VCS of *Tbx3:Tbx5* double-conditional heterozygous mice (*Tbx3<sup>fl/+</sup>;Tbx5<sup>fl/+</sup>;R26R<sup>eYFP/+</sup>;MinK<sup>CreERT2/+</sup>*) was observed compared to littermate controls (*Tbx3<sup>+/+</sup>;Tbx5<sup>+/+</sup>;R26R<sup>eYFP/+</sup>;MinK<sup>CreERT2/+</sup>*) (Figure 1C). We confirmed the specificity of the *Tbx3:Tbx5* double knockout for the VCS by assessing *Tbx3* and *Tbx5* expression levels in the atria and ventricles of tamoxifen-treated experimental mice. Consistent with the VCS selectivity of Cre activity in the *MinK<sup>CreERT2</sup>* mice (Arnolds and Moskowitz, 2011b), *Tbx3* and *Tbx5* expression remained similar in the atrial and ventricular myocardium of all allelic combinations, including *Tbx3:Tbx5* double-conditional knockout mice (*Tbx3<sup>fl/fl</sup>;Tbx5<sup>fl/fl</sup>;R26R<sup>eYFP/+</sup>;MinK<sup>CreERT2/+</sup>*) (Figure 1C).

*Tbx3:Tbx5* double-conditional knockout mice (*Tbx3<sup>fl/fl</sup>;Tbx5<sup>fl/fl</sup>;R26R<sup>eYFP/+</sup>;MinK<sup>CreERT2/+</sup>*) appeared morphologically and functionally normal and indistinguishable from control littermates (*Tbx3<sup>+/+</sup>;Tbx5<sup>+/+</sup>;R26R<sup>eYFP/+</sup>;MinK<sup>CreERT2/+</sup>*) at 2 weeks post-tamoxifen. However, longitudinal analysis demonstrated sudden death of VCS-specific double-knockout mice beginning 3 weeks post-tamoxifen administration (Figure 1D). Within the 3 months post-tamoxifen administration, all tamoxifen-treated *Tbx3<sup>fl/fl</sup>;Tbx5<sup>fl/fl</sup>;R26R<sup>eYFP/+</sup>;MinK<sup>CreERT2/+</sup>* mice had died suddenly ( $n = 40$ ). In contrast, no mortality was observed among the tamoxifen-treated *Tbx3<sup>+/+</sup>;Tbx5<sup>+/+</sup>;R26R<sup>eYFP/+</sup>;MinK<sup>CreERT2/+</sup>* or *Tbx3<sup>fl/+</sup>;Tbx5<sup>fl/+</sup>;R26R<sup>eYFP/+</sup>;MinK<sup>CreERT2/+</sup>* littermates (each cohort  $n = 40$ ) during this period (*Tbx3:Tbx5* double-conditional knockout mice vs. control mice  $p < 0.0001$ ; *Tbx3:Tbx5* double-conditional knockout mice vs. *Tbx3:Tbx5* double-conditional heterozygous mice  $p < 0.0001$ , log-rank test; Figure 1D). These results revealed that double deletion of *Tbx3* and *Tbx5* from the adult VCS causes lethality beginning at 3 weeks post-tamoxifen.

The onset of mortality observed in VCS-specific *Tbx3:Tbx5*-deficient mice starting at 3 weeks post-tamoxifen prompted us to investigate the electrophysiologic consequences of VCS-specific *Tbx3:Tbx5* double-knockout at 2–3 weeks post-tamoxifen, prior to the onset of lethality (Figure 2). VCS-specific *Tbx3:Tbx5* deficiency caused profound conduction slowing in *Tbx3<sup>fl/fl</sup>;Tbx5<sup>fl/fl</sup>;R26R<sup>eYFP/+</sup>;MinK<sup>CreERT2/+</sup>* mice by ambulatory telemetry electrocardiography (ECG) analysis compared to *Tbx3:Tbx5* double-conditional heterozygous mice (*Tbx3<sup>fl/+</sup>;Tbx5<sup>fl/+</sup>;R26R<sup>eYFP/+</sup>;MinK<sup>CreERT2/+</sup>*) and

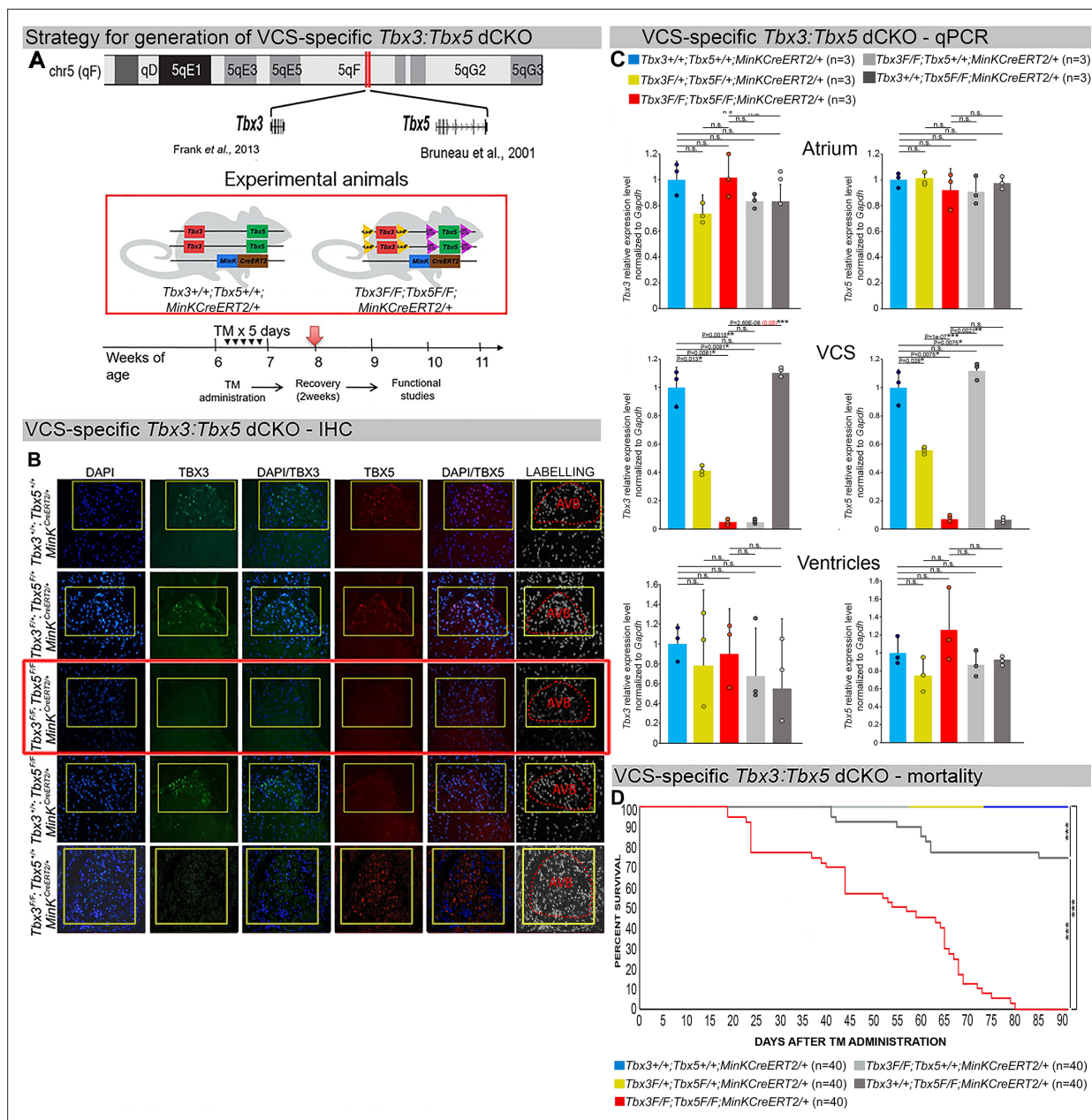


**Figure 1.** Generation of VCS-specific *Tbx3:Tbx5* double-conditional knockout mice. **(A)** Strategy to generate VCS-specific *Tbx3:Tbx5* double-conditional knockout mouse line. A new *Tbx3:Tbx5* double-conditional knockout mouse line ( $Tbx3^{fl/fl};Tbx5^{fl/fl}$ ) was generated using the CRISPR–Cas9 system (Gurumurthy et al., 2021; Dow et al., 2015) which allowed for the targeting of *Tbx5* in the background of the previously validated *Tbx3* floxed allele (Frank et al., 2011). A newly engineered *Tbx5* floxed allele has been developed to mirror a previously published allele (Bruneau et al., 2001). This design has enabled the utilization of the previously published individual *Tbx3* floxed allele (Frank et al., 2011) and individual *Tbx5* floxed allele (Bruneau et al., 2001) as controls. To conditionally delete *Tbx3* and *Tbx5* genes specifically from the adult VCS and generate the experimental animals, the *Tbx3:Tbx5* double-floxed mouse line ( $Tbx3^{fl/fl};Tbx5^{fl/fl}$ ) was combined with a VCS-specific tamoxifen inducible Cre transgenic mouse line (*MinK<sup>CreERT2</sup>* [Tg(RP23-276120-*MinKCreERT2*)] Arnolds and Moskowitz, 2011b). All allelic combinations were generated and evaluated as littermates in a mixed genetic background. The experimental mice employed in all studies were administered tamoxifen at 6 weeks of age and subsequently evaluated at 9 weeks of age (3 weeks post-tamoxifen administration). The loss of *Tbx3* and *Tbx5* expression, on both the protein and mRNA levels, assessed by immunohistochemistry **(B)** and qRT-PCR **(C)**, respectively, was observed in the VCS of adult *Tbx3:Tbx5* double-conditional mutant mice ( $Tbx3^{fl/fl};Tbx5^{fl/fl};R26^{eYFP/+};MinK^{CreERT2/+}$ ), but not in their littermate controls ( $Tbx3^{+/+};Tbx5^{+/+};R26^{eYFP/+};MinK^{CreERT2/+}$ ) **(B, C)**. **(C)** qRT-PCR analysis showed a partial loss of *Tbx3* and *Tbx5* expression in the adult VCS of *Tbx3:Tbx5* double-conditional heterozygous mice ( $Tbx3^{fl/+};Tbx5^{fl/+};R26^{eYFP/+};MinK^{CreERT2/+}$ ) compared to their littermate controls ( $Tbx3^{+/+};Tbx5^{+/+};R26^{eYFP/+};MinK^{CreERT2/+}$ ). Additionally, qRT-PCR analysis confirmed the specificity of the *Tbx3:Tbx5* double knockout for the VCS by assessing *Tbx3* and *Tbx5* expression levels in the atria and ventricles of tamoxifen-treated experimental mice. Consistent with the VCS selectivity of Cre activity in the *MinK<sup>CreERT2</sup>* mice (Arnolds and Moskowitz, 2011b), *Tbx3* and *Tbx5* expression remained similar in the atrial and

Figure 1 continued on next page



## Figure 1 continued

ventricular myocardium across all allelic combinations, including *Tbx3:Tbx5* double-conditional knockout mice (*Tbx3<sup>fl/fl</sup>;Tbx5<sup>fl/fl</sup>;R26R<sup>eYFP/+</sup>;Mink<sup>CreERT2/+</sup>*). (D) Conducted longitudinal studies revealed a significantly increased mortality rate in VCS-specific *Tbx3:Tbx5*-deficient mice compared to their littermate controls (\*\**p* < 0.0001, log-rank test, GraphPad Prism), suggesting a requirement for both *Tbx3* and *Tbx5* in the mature VCS. All allelic combinations of experimental and control mice (*n* = 40 biological replicates/genotype) were followed longitudinally after tamoxifen administration at 6 weeks of age. *Tbx3:Tbx5* double-conditional knockout mice began to die suddenly at 3–4 weeks post-tamoxifen administration. Within the 3 months post-tamoxifen administration, all tamoxifen-treated *Tbx3<sup>fl/fl</sup>;Tbx5<sup>fl/fl</sup>;R26R<sup>eYFP/+</sup>;Mink<sup>CreERT2/+</sup>* mice had died suddenly (*n* = 40) without previous signs of illness. In contrast, no mortality was observed among the tamoxifen-treated *Tbx3<sup>+/+</sup>;Tbx5<sup>+/+</sup>;R26R<sup>eYFP/+</sup>;Mink<sup>CreERT2/+</sup>* and *Tbx3<sup>fl/fl</sup>;Tbx5<sup>fl/fl</sup>;R26R<sup>eYFP/+</sup>;Mink<sup>CreERT2/+</sup>* littermates (each cohort *n* = 40) during this period. TBX3 and TBX5 protein expression was evaluated by immunohistochemistry (green and red signals, respectively) on serial sections from hearts of all allelic combinations (*n* = 3 biological replicates/genotype). Nuclei were stained with DAPI (blue signal). IHC original magnification: ×40. qRT-PCR data are presented as mean ± SD normalized to *Gapdh* and relative to *Tbx3<sup>+/+</sup>;Tbx5<sup>+/+</sup>;R26R<sup>eYFP/+</sup>;Mink<sup>CreERT2/+</sup>* mice (set as 1). *N* = 3 biological replicates/genotype (VCS cardiomyocytes pooled from 30 mice per biological replicate); multiple testing correction using Benjamini and Hochberg procedure. Significance was assessed by Welch *t*-test (\*FDR < 0.05; \*\*FDR < 0.005; \*\*\*FDR < 0.001) and confirmed by one-tailed Wilcoxon test (*p* value in parentheses) when normally distribution was rejected. Abbreviations: AVB, atrioventricular bundle (also known as bundle of His); FDR, false discovery rate; VCS, ventricular conduction system.

The online version of this article includes the following source data and figure supplement(s) for figure 1:

**Figure supplement 1.** Generation of a novel *Tbx5* floxed allele in a *Tbx3* floxed background.

**Figure supplement 1—source data 1.** File containing original gels corresponding to **Figure 1—figure supplement 1B**.

**Figure supplement 1—source data 2.** Zipped folder containing original gels corresponding to **Figure 1—figure supplement 1B**.

**Figure supplement 2.** Validation of the newly generated *Tbx5* floxed allele.

**Figure supplement 2—source data 1.** File containing original gels corresponding to **Figure 1—figure supplement 2B**.

**Figure supplement 2—source data 2.** Zipped folder containing original gels corresponding to **Figure 1—figure supplement 2B**.

**Figure supplement 3.** WT sequence of the targeted region at the mouse *Tbx5* locus.

**Figure supplement 4.** Sequence of long ssDNA donor designed to target exon 3 of the mouse *Tbx5* locus.

**Figure supplement 5.** Sequence of mouse new *Tbx5* floxed allele generated using CRISPR/Cas9 system with lssDNA composed of targeted exon 3 flanked by two lox2272 sites.

littermate controls (*Tbx3<sup>+/+</sup>;Tbx5<sup>+/+</sup>;R26R<sup>eYFP/+</sup>;Mink<sup>CreERT2/+</sup>*) (**Figure 2A–F**). Specifically, the PR interval, representing the period between atrial and ventricular depolarization, and the QRS duration, indicating the length of ventricular depolarization and early repolarization in mice, were both significantly prolonged (**Figure 2A, B, D**; PR: *Tbx3:Tbx5* double-conditional knockout mice vs. control mice *p* < 0.05, *n* = 7, Welch *t*-test; QRS: *Tbx3:Tbx5* double-conditional knockout mice vs. control mice *p* < 0.05, *n* = 7, Welch *t*-test). Removal of both *Tbx3* and *Tbx5* from the adult VCS resulted in increased episodes of spontaneous VT. Ambulatory studies revealed episodes of spontaneous VT in four out of seven *Tbx3<sup>fl/fl</sup>;Tbx5<sup>fl/fl</sup>;R26R<sup>eYFP/+</sup>;Mink<sup>CreERT2/+</sup>* mice, in contrast to none observed in seven littermate controls (**Figure 2G**, *p* < 0.05, *n* = 7, Welch *t*-test). Furthermore, *Tbx3:Tbx5* double-conditional knockout mice (*Tbx3<sup>fl/fl</sup>;Tbx5<sup>fl/fl</sup>;R26R<sup>eYFP/+</sup>;Mink<sup>CreERT2/+</sup>*) showed significantly increased susceptibility to VT following burst stimulation in invasive electrophysiology (EP) studies (three of three *Tbx3<sup>fl/fl</sup>;Tbx5<sup>fl/fl</sup>;R26R<sup>eYFP/+</sup>;Mink<sup>CreERT2/+</sup>* mice vs. zero of seven littermate controls; **Figure 2H**, *p* < 0.05, Welch *t*-test). In contrast, VCS-specific *Tbx3:Tbx5* double-conditional heterozygous mice (*n* = 7) showed neither conduction nor electrophysiological defects (**Figure 2**). Consistent with the use of a VCS-specific *Cre* (*Mink<sup>CreERT2</sup>*), no changes in the refractory/recovery periods of atrium, ventricle, or nodes (atrial effective refractory period, ventricular effective refractory period (VERP), atrioventricular nodal effective refractory period, or sinus node recovery time) were detected by intracardiac EP conducted on experimental and control mice (**Figure 2I**, *p* < 0.05, Welch *t*-test).

To distinguish a primary conduction system abnormality from a secondary conduction abnormality resulting from cardiac dysfunction or remodeling, we evaluated cardiac form and function at the time of arrhythmia assessment, 2–3 weeks post-tamoxifen treatment (**Figure 3**). Transthoracic echocardiography revealed no significant differences in left ventricular ejection fraction (LVEF) and fractional shortening (FS) between VCS-specific *Tbx3:Tbx5*-deficient (*Tbx3<sup>fl/fl</sup>;Tbx5<sup>fl/fl</sup>;R26R<sup>eYFP/+</sup>;Mink<sup>CreERT2/+</sup>*) and control (*Tbx3<sup>+/+</sup>;Tbx5<sup>+/+</sup>;R26R<sup>eYFP/+</sup>;Mink<sup>CreERT2/+</sup>*) mice (LVEF: *Tbx3:Tbx5* double-conditional knockout mice vs. control mice *p* < 0.05, *n* = 7, Welch *t*-test; and FS: *Tbx3:Tbx5* double-conditional knockout mice vs. control mice *p* > 0.05, *n* = 7, Welch *t*-test; **Figure 3A, B, D**). Histological examination of all four chambers demonstrated no discernible differences between VCS-specific *Tbx3:Tbx5* double-knockout

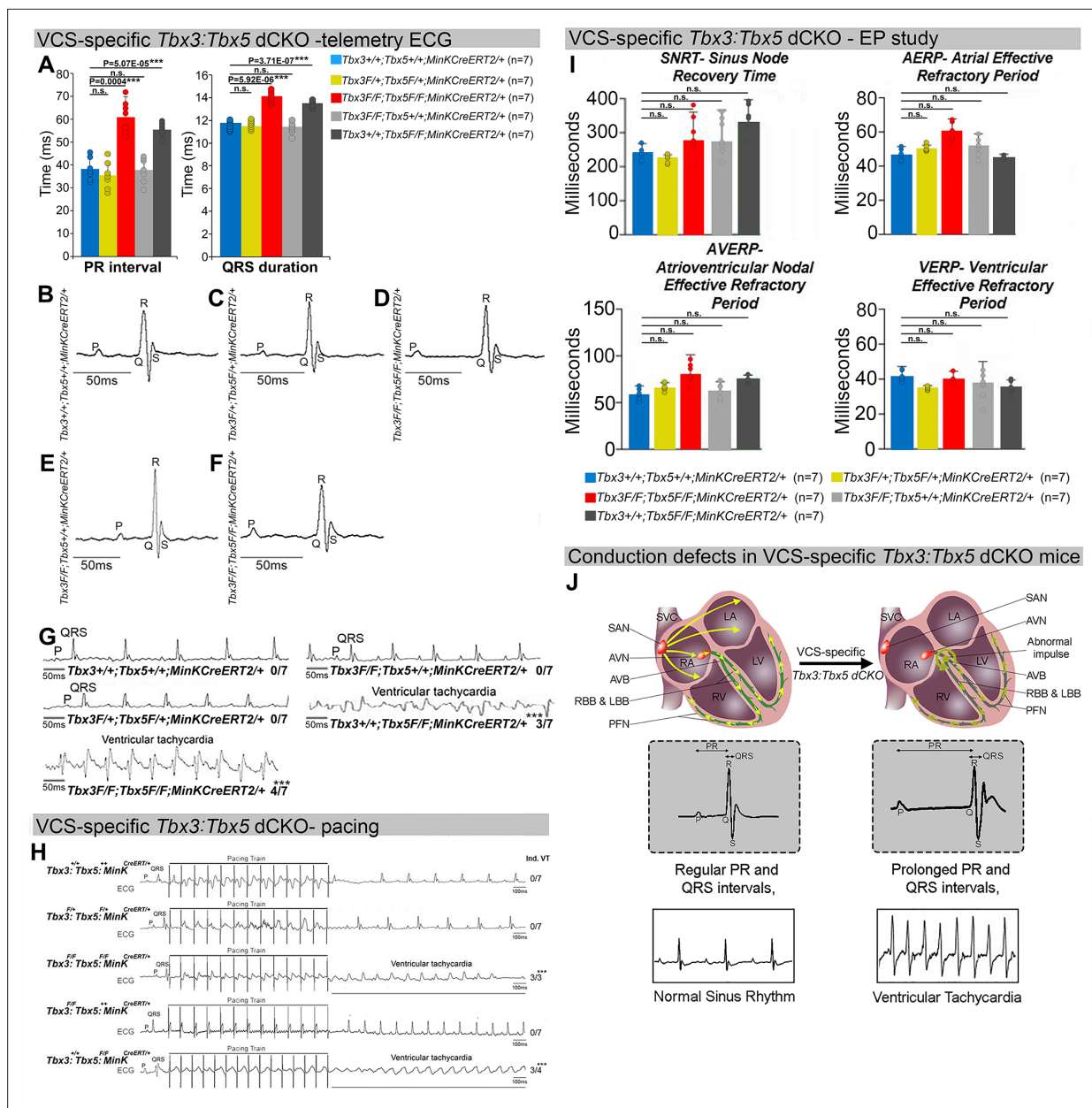


**Figure 2.** Arrhythmias and conduction abnormalities in mice with VCS-specific *Tbx3:Tbx5* double-conditional knockout. **(A–F)** VCS-specific *Tbx3:Tbx5* double-conditional knockout causes significant VCS conduction slowing in adult *Tbx3*<sup>fl/fl</sup>;*Tbx5*<sup>fl/fl</sup>;*R26R*<sup>eYFP/+</sup>;*MinK*<sup>CreERT2/+</sup> mice. **(A)** PR (left graph) and QRS (right graph) intervals calculated from ambulatory telemetry electrocardiography (ECG) recordings in **(B–F)**. *Tbx3:Tbx5* double-conditional adult mice (*Tbx3*<sup>fl/fl</sup>;*Tbx5*<sup>fl/fl</sup>;*R26R*<sup>eYFP/+</sup>;*MinK*<sup>CreERT2/+</sup>) displayed significant PR and QRS intervals prolongation compared to littermate controls (*Tbx3*<sup>+/+</sup>;*Tbx5*<sup>+/+</sup>;*R26R*<sup>eYFP/+</sup>;*MinK*<sup>CreERT2/+</sup>) (A left and right graphs, respectively). Data are presented as mean ± SD. N = 7 biological replicates/genotype; multiple testing correction using Benjamini and Hochberg procedure; \*Welch t-test  $p < 0.05$  and FDR < 0.05; \*\*Welch t-test  $p < 0.005$  and FDR < 0.05; \*\*\*Welch t-test  $p < 0.001$  and FDR < 0.05. Representative ambulatory telemetry ECG of *Tbx3*<sup>fl/fl</sup>;*Tbx5*<sup>fl/fl</sup>;*R26R*<sup>eYFP/+</sup>;*MinK*<sup>CreERT2/+</sup> **(B)**, *Tbx3*<sup>fl/fl</sup>;*Tbx5*<sup>+/+</sup>;*R26R*<sup>eYFP/+</sup>;*MinK*<sup>CreERT2/+</sup> **(C)**, *Tbx3*<sup>+/+</sup>;*Tbx5*<sup>fl/fl</sup>;*R26R*<sup>eYFP/+</sup>;*MinK*<sup>CreERT2/+</sup> **(D)**, *Tbx3*<sup>fl/fl</sup>;*Tbx5*<sup>+/+</sup>;*R26R*<sup>eYFP/+</sup>;*MinK*<sup>CreERT2/+</sup> **(E)**, *Tbx3*<sup>+/+</sup>;*Tbx5*<sup>fl/fl</sup>;*R26R*<sup>eYFP/+</sup>;*MinK*<sup>CreERT2/+</sup> **(F)** mice. **(G)** Simultaneous genetic removal of *Tbx3* and *Tbx5* from the adult VCS resulted in significantly increased episodes of spontaneous ventricular tachycardia. Episodes of spontaneous ventricular tachycardia were observed in four of seven *Tbx3*<sup>fl/fl</sup>;*Tbx5*<sup>fl/fl</sup>;*R26R*<sup>eYFP/+</sup>;*MinK*<sup>CreERT2/+</sup> mice versus zero of seven littermate controls (*Tbx3*<sup>+/+</sup>;*Tbx5*<sup>+/+</sup>;*R26R*<sup>eYFP/+</sup>;*MinK*<sup>CreERT2/+</sup>) in ambulatory studies. N = 7 biological replicates/genotype; multiple testing correction using Benjamini and Hochberg procedure; \*FDR of Welch t-test  $\leq 0.05$ . **(H)** *Tbx3:Tbx5* double-conditional knockout mice (*Tbx3*<sup>fl/fl</sup>;*Tbx5*<sup>fl/fl</sup>;*R26R*<sup>eYFP/+</sup>;*MinK*<sup>CreERT2/+</sup>) showed significantly increased susceptibility to ventricular tachycardia following burst stimulation in invasive electrophysiology studies (three of three *Tbx3*<sup>fl/fl</sup>;*Tbx5*<sup>fl/fl</sup>;*R26R*<sup>eYFP/+</sup>;*MinK*<sup>CreERT2/+</sup> mice vs. zero of seven control *Tbx3*<sup>+/+</sup>;*Tbx5*<sup>+/+</sup>;*R26R*<sup>eYFP/+</sup>;*MinK*<sup>CreERT2/+</sup> mice. Fisher's exact test: \* $p < 0.05$ ; n = 7 biological replicates/genotype). **(I)** Intracardiac electrophysiology detected no significant changes in SNRT, AERP, AVERP, and VERP recorded from experimental and control animals (n = 7 biological replicates/genotype; multiple testing correction using Benjamini

Figure 2 continued on next page

## Figure 2 continued

and Hochberg procedure; \*FDR of Welch t-test  $\leq 0.05$ ). (J) Graphical summary of conduction defects observed in adult, VCS-specific *Tbx3:Tbx5*-deficient mice. Simultaneous genetic deletion of *Tbx3* and *Tbx5* from the mature VCS results in conduction slowing, prolonged PR and QRS intervals, as well as ventricular tachycardia. Abbreviations: AVB, atrioventricular bundle (also known as bundle of His); AVN, atrioventricular node; FDR, false discovery rate; LA, left atrium; LBB, left bundle branches; LV, left ventricle; PFN, Purkinje fiber network; RA, right atrium; RBB, right bundle branches; RV, right ventricle; SAN, sinoatrial node; SVC, superior vena cava; VCS, ventricular conduction system.

(*Tbx3<sup>fl/fl</sup>;Tbx5<sup>fl/fl</sup>;R26R<sup>eYFP/+</sup>;Mink<sup>CreERT2/+</sup>*) and control (*Tbx3<sup>+/+</sup>;Tbx5<sup>+/+</sup>;R26R<sup>eYFP/+</sup>;Mink<sup>CreERT2/+</sup>*) mice, nor between the double-knockout (*Tbx3<sup>fl/fl</sup>;Tbx5<sup>fl/fl</sup>;R26R<sup>eYFP/+</sup>;Mink<sup>CreERT2/+</sup>*) and single-knockout models for either *Tbx3* (*Tbx3<sup>fl/fl</sup>;Tbx5<sup>+/+</sup>;R26R<sup>eYFP/+</sup>;Mink<sup>CreERT2/+</sup>*) or *Tbx5* (*Tbx3<sup>+/+</sup>;Tbx5<sup>fl/fl</sup>;R26R<sup>eYFP/+</sup>;Mink<sup>CreERT2/+</sup>*). Ventricular muscle appeared normal without hypertrophy or myofibrillar disarray, and no fibrosis was present (Figure 3G, I–K, respectively). qRT-PCR analysis for fibrosis genes *Col1a1* (Pan et al., 2022; Hua et al., 2020; Zhao et al., 2018) and *Postn* (Zhao et al., 2018; Ackerman et al., 2024; Wu et al., 2024; Oka et al., 2007) further confirmed no fibrosis in VCS of *Tbx3:Tbx5*-deficient mice (Figure 3L). No contractile dysfunction, histological abnormalities, or increased expression of fibrosis genes were observed in VCS-specific *Tbx3:Tbx5* double-conditional heterozygous mice (*Tbx3<sup>fl/+</sup>;Tbx5<sup>fl/+</sup>;R26R<sup>eYFP/+</sup>;Mink<sup>CreERT2/+</sup>*) (Figure 3A, C, H, L). Taken together, these data indicate that the conduction defect and VT observed in mice with VCS-specific *Tbx3:Tbx5* deletion (Figure 2) occur prior to the onset of left ventricular (LV) dysfunction or evidence of remodeling (Figure 3), implying a primary origin.

To assess the hypothesis that *Tbx3* and *Tbx5* collectively promote VCS versus working myocardium phenotype, we conducted a transcriptional characterization of the adult VCS in *Tbx3<sup>fl/fl</sup>;Tbx5<sup>fl/fl</sup>;R26R<sup>eYFP/+</sup>;Mink<sup>CreERT2/+</sup>* mutant mice compared to their *Tbx3<sup>+/+</sup>;Tbx5<sup>+/+</sup>;R26R<sup>eYFP/+</sup>;Mink<sup>CreERT2/+</sup>* control littermates using three distinct sets of molecular markers by qRT-PCR (Figure 4A–C). The first set encompassed genes expressed throughout the entire conduction system (Pan-CCS) and implicated in slow-conducting nodal phenotype, such as *Hcn1*, *Hcn4*, *Cacna1d* (Cav1.3), *Cacna1g* (Cav3.1d), *Cacna1h* (Cav3.2), *Gjd3* (Cx30.2), and *Gjc1* (Cx45) (Bakker et al., 2012; Hoogaars et al., 2004; van Eif et al., 2020; Verheule and Kaese, 2013; Liang et al., 2013; Greener et al., 2011; Mangoni et al., 2006; Marionneau et al., 2005; Garcia-Frigola et al., 2003; Schram et al., 2002; Figure 4A). The second set included genes highly expressed in the fast-conducting VCS and important for VCS function, including *Gja5* (Cx40), *Scn5a* (Nav1.5), *Ryr2*, *Kcnk3* (Task-1), *Kcnj2* (Kir2.1), *Kcnj3* (Kir3.1), *Kcnj4* (IRK3), and *Kcnj12* (Kir2.2) (Figure 4B; van Eif et al., 2020; Verheule and Kaese, 2013; Schram et al., 2002; Donner et al., 2011; Miquelot et al., 2010; Remme et al., 2009; Graham et al., 2006). The third set contained markers specifically present in the working myocardium but absent in the CCS, such as *Gja1* (Cx43) and *Smpx* (Figure 4C; Hoogaars et al., 2004; van Eif et al., 2020; Alcoléa et al., 1999; Kempen et al., 1996). VCS-specific *Tbx3:Tbx5*-deficient mice lost VCS expression profile of genes required for the fast ventricular conduction (Figure 4B) as well as genes normally expressed in whole CCS (Pan-CCS genes) (Figure 4A). In contrast, these mice obtained VCS expression of working myocardium-specific molecular markers (Figure 4C). Immunoblotting analysis confirmed transcriptional changes observed by qRT-PCR (Figure 4D). This molecular characterization indicated that the *Tbx3:Tbx5* double mutant VCS adopted a gene expression profile similar to wild-type working myocardial-like cells (Figure 4).

The impact of the *Tbx3:Tbx5* double-conditional knockout on electrical impulse propagation in the VCS of the heart was assessed with optical mapping of the anterior epicardial surface of the ventricles and right septal preparations where VCS function should be observed (Figure 5). Optical mapping records changes in transmembrane potential from multiple cells in tissue preparations, where ventricular septal optical action potentials (OAPs) have two distinct action potential upstrokes. The first peak is a result of depolarization of the specialized fast VCS, followed by depolarization of ventricular working myocardium.

To visualize electrical impulse propagation in *Tbx3:Tbx5* double-conditional knockout mice, a 100 × 100 pixel data frame was plotted for the entire field of view of the right septal preparation (Figure 5A, B). For enhanced analysis of the VCS, the region encompassing the His bundle was distinguished in a red 10 × 10 area (Figure 5B). To specifically assess electrical impulse propagation within the His bundle, the same 10 × 10 pixel area representing this region was isolated from adult hearts of both control and *Tbx3:Tbx5* double-conditional knockout mice (Figure 5C). We observed only one OAP upstroke in *Tbx3:Tbx5* double-conditional knockout mice in contrast to control mice which showed two



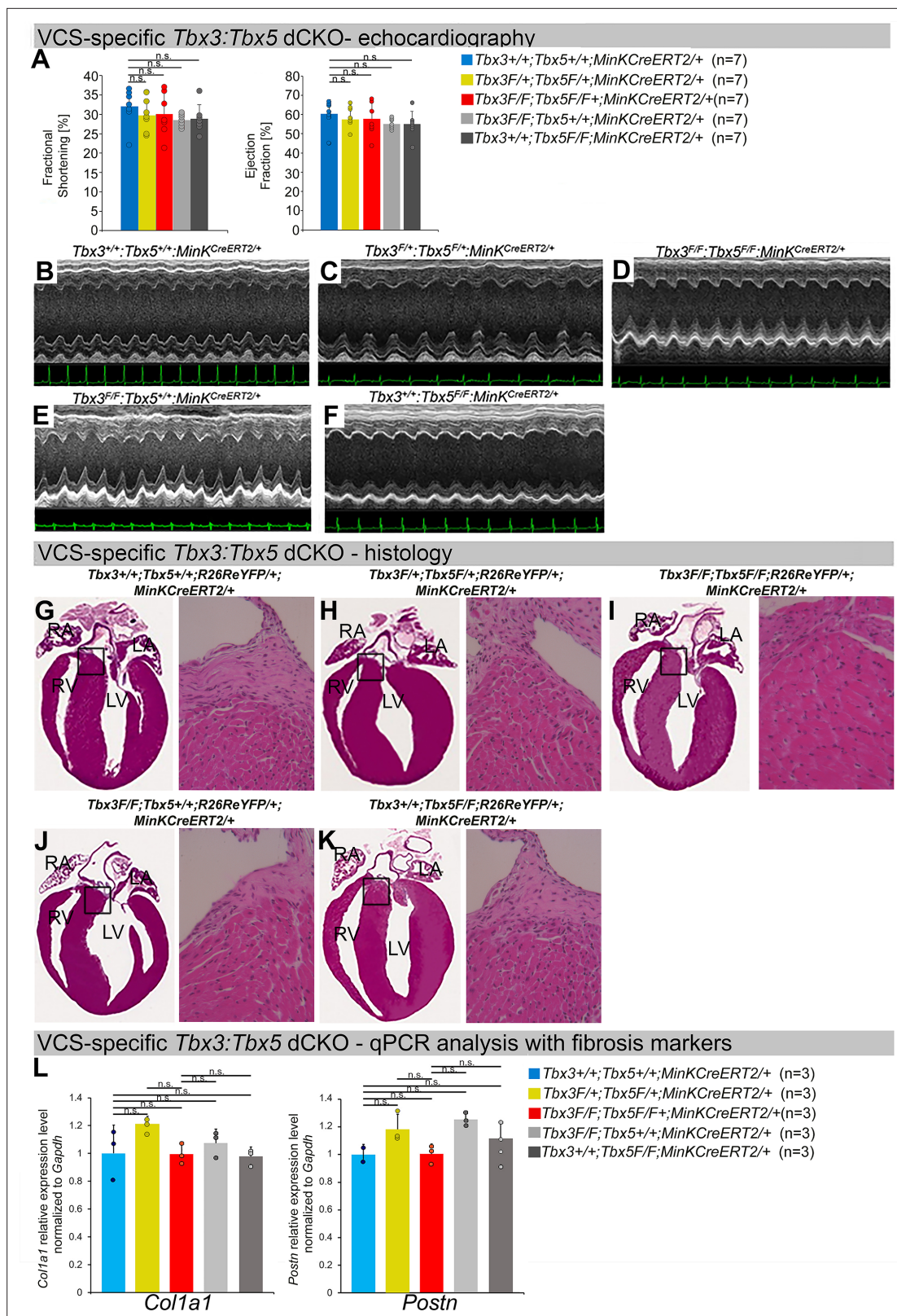


**Figure 3.** Cardiac function is preserved following double-conditional loss of *Tbx3* and *Tbx5* in the adult ventricular conduction system (VCS). (A) Left ventricular (LV) fractional shortening (left graph) and LV ejection fraction (right graph) calculated from the M-mode electrocardiographies (ECGs) in (B–F) revealed no contractile dysfunction in VCS-specific *Tbx3:Tbx5* double-conditional mutant mice (*Tbx3*<sup>F/F</sup>;*Tbx5*<sup>F/F</sup>;*R26ReYFP*<sup>+/+</sup>;*MinKCreERT2*<sup>+/+</sup>). Data are presented as mean ± SD. Welch t-test: ns, not significant ( $p > 0.05$ );  $n = 7$  biological replicates/genotype. (B–F) Cardiac function, assessed by M-mode

Figure 3 continued on next page



## Figure 3 continued

echocardiography from *Tbx3<sup>+/+</sup>;Tbx5<sup>+/+</sup>;R26R<sup>eYFP/+</sup>;MinK<sup>CreERT2/+</sup>* (B), *Tbx3<sup>fl/+</sup>;Tbx5<sup>fl/+</sup>;R26R<sup>eYFP/+</sup>;MinK<sup>CreERT2/+</sup>* (C), *Tbx3<sup>fl/fl</sup>;Tbx5<sup>fl/fl</sup>;R26R<sup>eYFP/+</sup>;MinK<sup>CreERT2/+</sup>* (D), *Tbx3<sup>fl/fl</sup>;Tbx5<sup>+/+</sup>;R26R<sup>eYFP/+</sup>;MinK<sup>CreERT2/+</sup>* (E), *Tbx3<sup>+/+</sup>;Tbx5<sup>fl/fl</sup>;R26R<sup>eYFP/+</sup>;MinK<sup>CreERT2/+</sup>* (F) mice shown above surface ECGs. No functional differences between mutant and control mice were detected. The most representative images for each genotype were utilized in the figure.  $n = 7$  biological replicates/genotype. (G–K) Histological examination of all four chambers from *Tbx3<sup>+/+</sup>;Tbx5<sup>+/+</sup>;R26R<sup>eYFP/+</sup>;MinK<sup>CreERT2/+</sup>* (G), *Tbx3<sup>fl/+</sup>;Tbx5<sup>fl/+</sup>;R26R<sup>eYFP/+</sup>;MinK<sup>CreERT2/+</sup>* (H), *Tbx3<sup>fl/fl</sup>;Tbx5<sup>fl/fl</sup>;R26R<sup>eYFP/+</sup>;MinK<sup>CreERT2/+</sup>* (I), *Tbx3<sup>fl/fl</sup>;Tbx5<sup>+/+</sup>;R26R<sup>eYFP/+</sup>;MinK<sup>CreERT2/+</sup>* (J), *Tbx3<sup>+/+</sup>;Tbx5<sup>fl/fl</sup>;R26R<sup>eYFP/+</sup>;MinK<sup>CreERT2/+</sup>* (K) mice showed no histological abnormalities. The most representative images for each genotype were utilized in the figure.  $n = 3–4$  biological replicates/genotype. Boxed areas in (G–K) have been shown at higher magnification at their right sides. (L) qRT-PCR analysis for fibrosis genes *Col1a1* and *Postn* confirmed that there was no increase in expression of fibrosis markers in the VCS of *Tbx3;Tbx5*-deficient mice. Data are presented as mean  $\pm$  SD normalized to *Gapdh* and relative to *Tbx3<sup>+/+</sup>;Tbx5<sup>+/+</sup>;R26R<sup>eYFP/+</sup>;MinK<sup>CreERT2/+</sup>* mice (set as 1). ns: FDR  $>0.05$  in both Welch t-test and Wilcoxon test;  $n = 2–3$  biological replicates/genotype (VCS cardiomyocytes pooled from 30 mice per biological replicate). Histological examination original magnification:  $\times 2.5$ , boxed area showed at the higher magnification:  $\times 40$ . Abbreviations: FDR, false discovery rate; LA, left atrium; RA, right atrium; LV, left ventricle; RV, right ventricle.

OAP upstrokes. The first derivative of the OAP (dOAP/dt) from the region of the His bundle was calculated and plotted in a dOAP/dt map further highlighting the number of temporally distinct upstrokes within the OAP (Figure 5D). In control mice, we observed two distinct depolarization upstrokes, one pertaining to the VCS and the second for working ventricular myocardium. However, in *Tbx3;Tbx5* double-conditional knockout mice, only one maximum dOAP/dt was observed (Figure 5D). The OAP morphology observed in *Tbx3;Tbx5* double-conditional knockout mice suggested a loss or reduction of the specialized fast VCS conduction (Figure 5C, D).

OAPs from the anterior epicardial surface of the ventricles were compared between control littermates and *Tbx3;Tbx5* double-conditional knockout mice to assess changes in electrical impulse propagation in the ventricular working myocardium. Paced at a basic cycle length of 125 ms, control littermates and *Tbx3;Tbx5* double-conditional knockout mice did not exhibit significant differences in action potential duration at 50% (APD50) or 80% (APD80) repolarization (Figure 5E, F). These observations suggested that the electrical activity of the ventricular working myocardium was not appreciably altered in double-knockout mice compared to controls. This finding is consistent with the lack of changes in the VERP observed in invasive EP studies of both control and *Tbx3;Tbx5* double-conditional knockout mice (Figure 3I).

We further predicted that the double knockout would not affect action potentials or conduction properties distal to the VCS (Figure 6). OAP and dOAP/dt maps were created to observe the effects on electrical impulse propagation distal to the His bundle on the right septal preparation (Figure 6), similar to the methods applied to create OAP and dOAP/dt maps in the region of the His bundle (Figure 5), with the key difference being that the signals were recorded from the red  $10 \times 10$  pixel regions plotted in the working ventricular myocardium distal to the His bundle instead of in the area of the His bundle (Figure 6A, B vs. Figure 5A, B, respectively). In both control littermates and *Tbx3;Tbx5* double-conditional knockout mice, only one action potential upstroke and one dOAP/dt maximum are observed, which indicates that most of this region consists of the ventricular working myocardium (Figure 6C and D, respectively). In summary, the significant remodeling of electrical impulse propagation due to *Tbx3;Tbx5* double-conditional knockout was observed by the loss of a distinct fast VCS impulse in the region of the His bundle, but not on the anterior epicardial surface of the ventricles or distal to the His bundle on the right ventricular (RV) septum (Figures 5 and 6).

## Discussion

Our study investigated the impact of compound *Tbx3;Tbx5* deficiency on mature VCS function and molecular identity. Using a double-conditional knockout strategy, both genes were targeted specifically in the adult VCS. Loss of *Tbx3* and *Tbx5* expression in the mature VCS led to profound conduction defects, characterized by prolonged PR interval and QRS duration, increased susceptibility to VT, and sudden death. These alterations were observed in the absence of discernible changes in cardiac contractility or histological morphology, indicating a primary conduction system defect. Molecular characterization of the adult VCS unveiled an altered gene expression profile in *Tbx3;Tbx5* double-conditional knockout mice, suggesting a transition from the distinctive fast VCS transcriptional profile to that resembling ventricular working myocardium. Optical mapping demonstrated loss of the specialized fast VCS function in *Tbx3;Tbx5* double-conditional knockout mice, further suggesting that this region acquired an electrophysiological phenotype similar to the ventricular working myocardium.

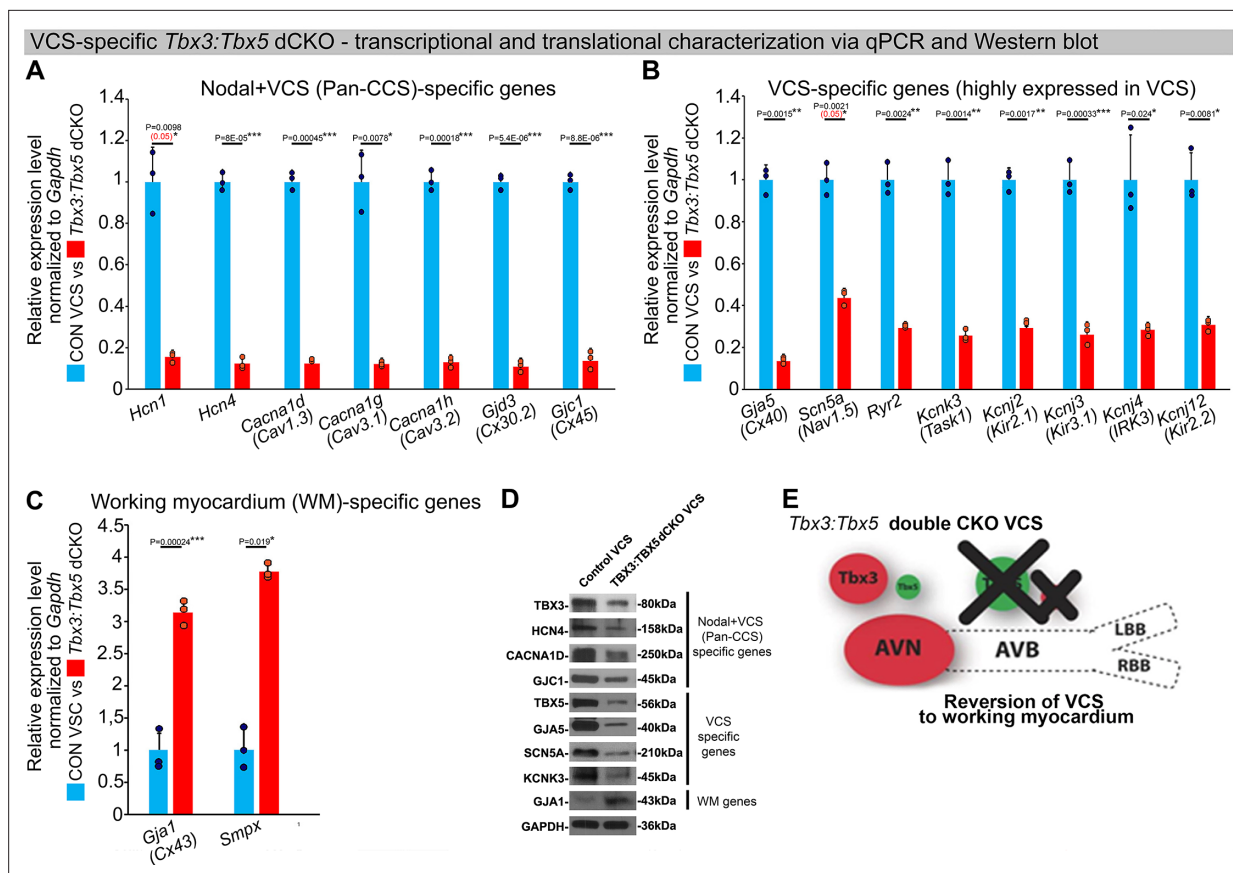


**Figure 4.** In the adult murine heart, *Tbx3* and *Tbx5* collectively promote ventricular conduction system (VCS) versus working myocardium (WM) phenotype. (A–C) qRT-PCR analysis of molecular changes driven by VCS-specific *Tbx3:Tbx5* double-conditional knockout in adult mice. Transcriptional characterization of the adult VCS in *Tbx3<sup>fl/fl</sup>;Tbx5<sup>fl/fl</sup>;R26R<sup>YFP/+</sup>;MinK<sup>CreERT2/+</sup>* mutant mice, compared to their *Tbx3<sup>+/+</sup>;Tbx5<sup>+/+</sup>;R26R<sup>YFP/+</sup>;MinK<sup>CreERT2/+</sup>* control littermates, was conducted using three distinct sets of molecular markers. (A) Genes expressed throughout the entire conduction system (Pan-CCS), implicated in the slow-conducting nodal phenotype. (B) Genes highly expressed in the fast-conducting VCS, critical for VCS function. (C) Markers specifically present in the working myocardium but absent in the CCS. VCS-specific *Tbx3:Tbx5*-deficient mice lost the VCS expression profile, including genes necessary for fast ventricular conduction (B) and those typically expressed in the entire CCS (Pan-CCS genes), essential for the slow-conducting nodal phenotype (A). In contrast, they acquired VCS expression of working myocardium-specific molecular markers important for working myocardial function (C). (D) Immunoblotting analysis confirmed transcriptional changes indicated by qRT-PCR analysis (A–C) in VCS-specific *Tbx3:Tbx5* double-conditional knockout in adult mice. (E) Graphical summary of transcriptional changes observed in VCS of VCS-specific *Tbx3:Tbx5*-deficient mice. Simultaneous genetic deletion of *Tbx3* and *Tbx5* from the mature VCS resulted in a transcriptional profile resembling that of ventricular working myocardium. qRT-PCR data are presented as mean  $\pm$  SD normalized to *Gapdh* and relative to *Tbx3<sup>+/+</sup>;Tbx5<sup>+/+</sup>;R26R<sup>YFP/+</sup>;MinK<sup>CreERT2/+</sup>* mice (set as 1).  $N = 3$  biological replicates/genotype (VCS cardiomyocytes pooled from 30 mice per biological replicate); multiple testing correction using Benjamini and Hochberg procedure. Significance was assessed by Welch t-test (\*FDR < 0.05; \*\*FDR < 0.005; \*\*\*FDR < 0.001) and confirmed by one-tailed Wilcoxon test (p value in parentheses) when normal distribution was rejected. Western blotting,  $n = 2$  biological replicates/genotype (VCS cardiomyocytes pooled from 50 mice per each biological replicate). Abbreviations: AVB, atrioventricular bundle (also known as bundle of His); AVN, atrioventricular node; dCKO, double-conditional knockout; FDR, false discovery rate; LBB, left bundle branches; RBB, right bundle branches; VCS, ventricular conduction system.

The online version of this article includes the following source data for figure 4:

**Source data 1.** File containing original western blots corresponding to **Figure 4D**.

**Source data 2.** Zipped folder containing original western blots files corresponding to **Figure 4D**.

Our previous research (Arnolds et al., 2012; Moskowitz et al., 2007; Burnicka-Turek et al., 2020; Moskowitz et al., 2004) and published literature van Duijvenboden et al., 2014; Bakker et al., 2012; Bruneau et al., 2001; Frank et al., 2011; Mohan et al., 2020; van Eif et al., 2018 have suggested that the balance between *Tbx3* and *Tbx5* expression determines the regional specialization of the mature central CCS (Figure 7). *Tbx3* expression dominates in nodal myocardium, imparting nodal physiological characteristics. *Tbx5* expression dominates in fast VCS myocardium, where a T-box-dependent fast conduction system network drives physiologically dominant fast conduction

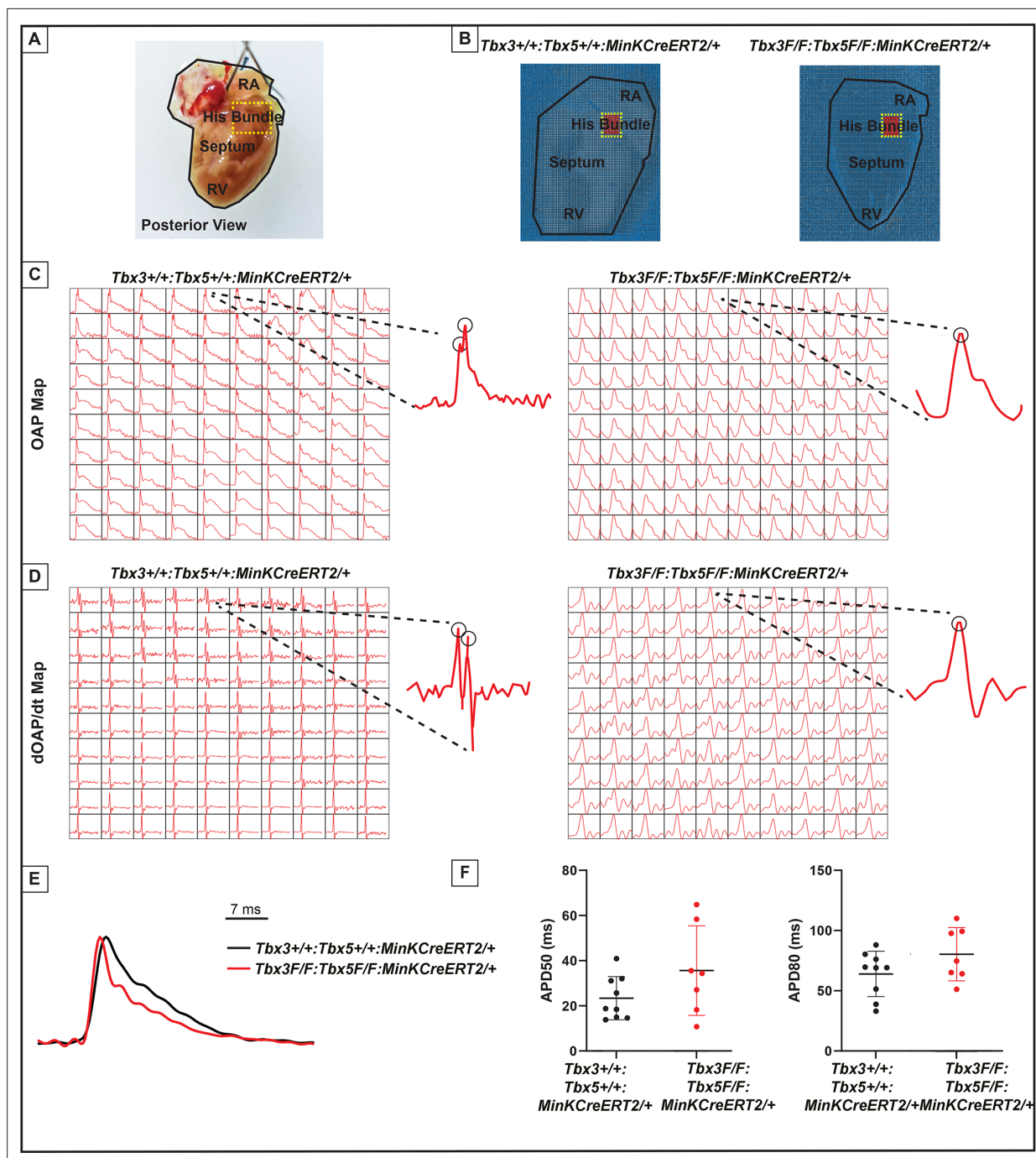


**Figure 5.** Loss of VCS optical action potential (OAP) morphology in *Tbx3*:*Tbx5* double-conditional knockout mice. **(A)** Schematic of the posterior view of a mouse heart with right ventricle (RV) free wall removed, highlighting the RV, septum, His bundle, and right atria (RA). **(B)** Representative 100 × 100 OAP map of OAP recorded during sinus rhythm from *Tbx3*:*Tbx5* double-conditional knockout mice and control littermates with the free wall removed. The region of the His bundle is highlighted in red. **(C)** Representative 10 × 10 OAP map from the region of the His bundle. **(D)** Representative 10 × 10 map of the first derivative of the OAP from the region of the His bundle. **(E)** Representative ventricular OAP from whole heart intact preparation from *Tbx3*:*Tbx5* double-conditional knockout mice (red) and control littermates (black). **(F)** Quantification of APD50 and APD80 at a basic cycle length of 125 ms. For (C-F), n=10 or 8 animals/ genotype.

The online version of this article includes the following figure supplement(s) for figure 5:

**Figure supplement 1.** *Tbx3*:*Tbx5* double-conditional knockout mice exhibit QRS prolongation.

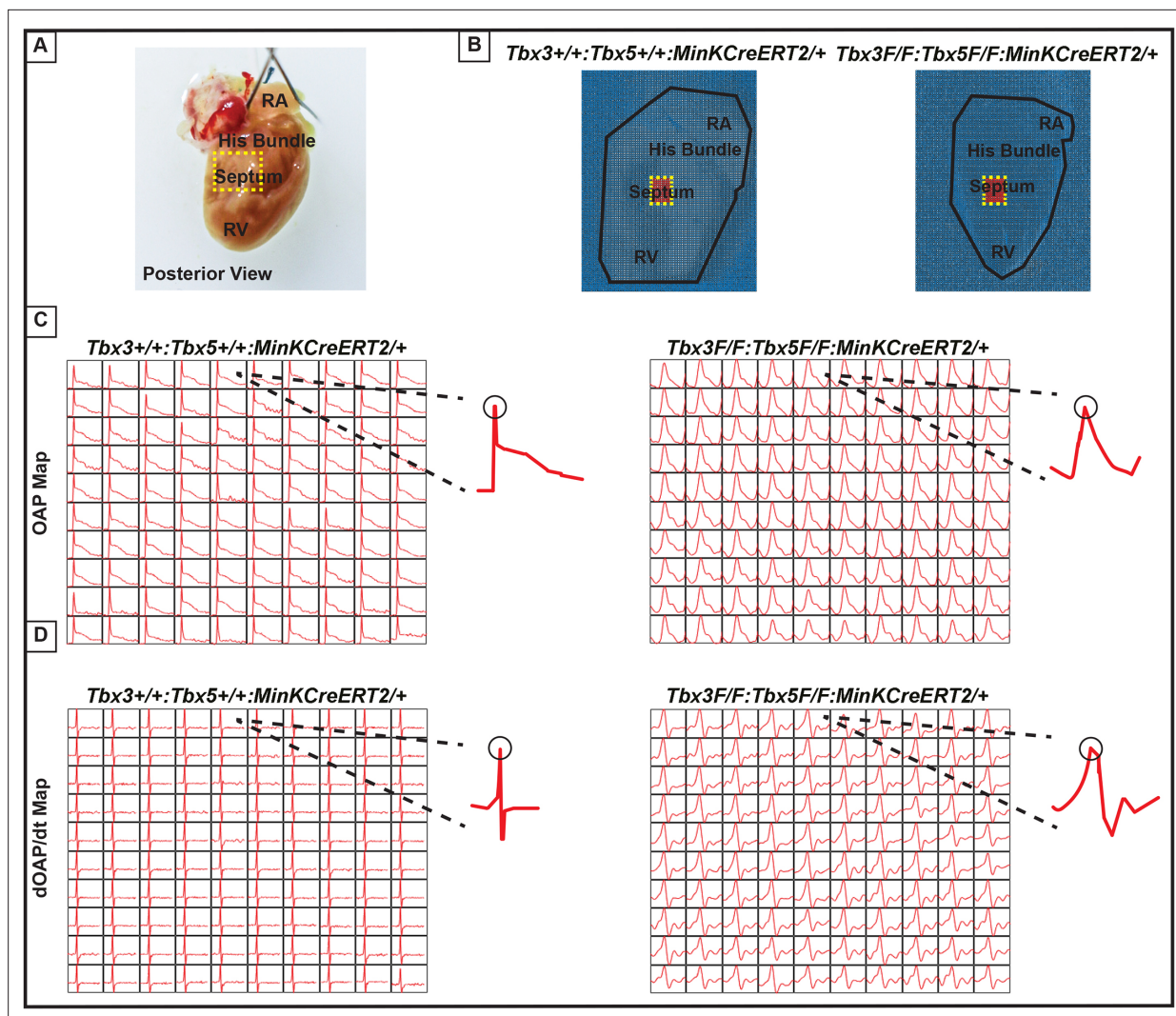


**Figure 6.** Ventricular optical action potentials (OAPs) distal from His bundle have only one OAP upstroke. (A) Schematic of the posterior view of mouse heart with right ventricle (RV) free wall removed. (B) Representative 100 × 100 pixel OAP map recorded during sinus rhythm from *Tbx3:Tbx5* double-conditional knockout mice and control littermates with RV free wall removed. The region of the working ventricular myocardium distal from the His bundle is highlighted in red. (C) Representative 10 × 10 pixel OAP map from the region distal to the His bundle. (D) Representative 10 × 10 dOAP/dt map from the region distal to the His bundle. For (C and D), n=10 or 8 animals/genotype.

physiology, overriding nodal physiology (Burnicka-Turek et al., 2020; Figure 7). This model accurately predicts the outcome of targeted manipulations, such as adult VCS-specific removal of TBX5 or overexpression of TBX3, which convert the fast VCS into a slow nodal-like system (Burnicka-Turek et al., 2020; Figure 7).

The adult CCS organization model posits that *Tbx3* and *Tbx5* coordinately establish CCS characteristics and suggests their compound necessity to maintain specialized VCS identity (Figure 7), a hypothesis that remained untested. This model predicted that VCS-specific genetic ablation of both the TBX3 and TBX5 transcription factors would transform fast-conducting adult VCS into cells resembling working myocardium, eliminating specialized CCS identity (Figure 7). Testing this model necessitated the generation of a *Tbx3:Tbx5* double-conditional knockout allele due to their proximal chromosomal location in cis on mouse Chr5. VCS-specific double-knockout mice showed a notable deceleration in VCS conduction, manifested by prolonged PR and QRS intervals, along with increased susceptibility to VT. A similar functional phenotype was observed in single deletion of *Tbx5* from the adult VCS, leading to the transformation of the fast VCS into a nodal-like phenotype (Arnolds et al., 2012; Burnicka-Turek et al., 2020). However, we predicted that the nodal-like characteristics of the



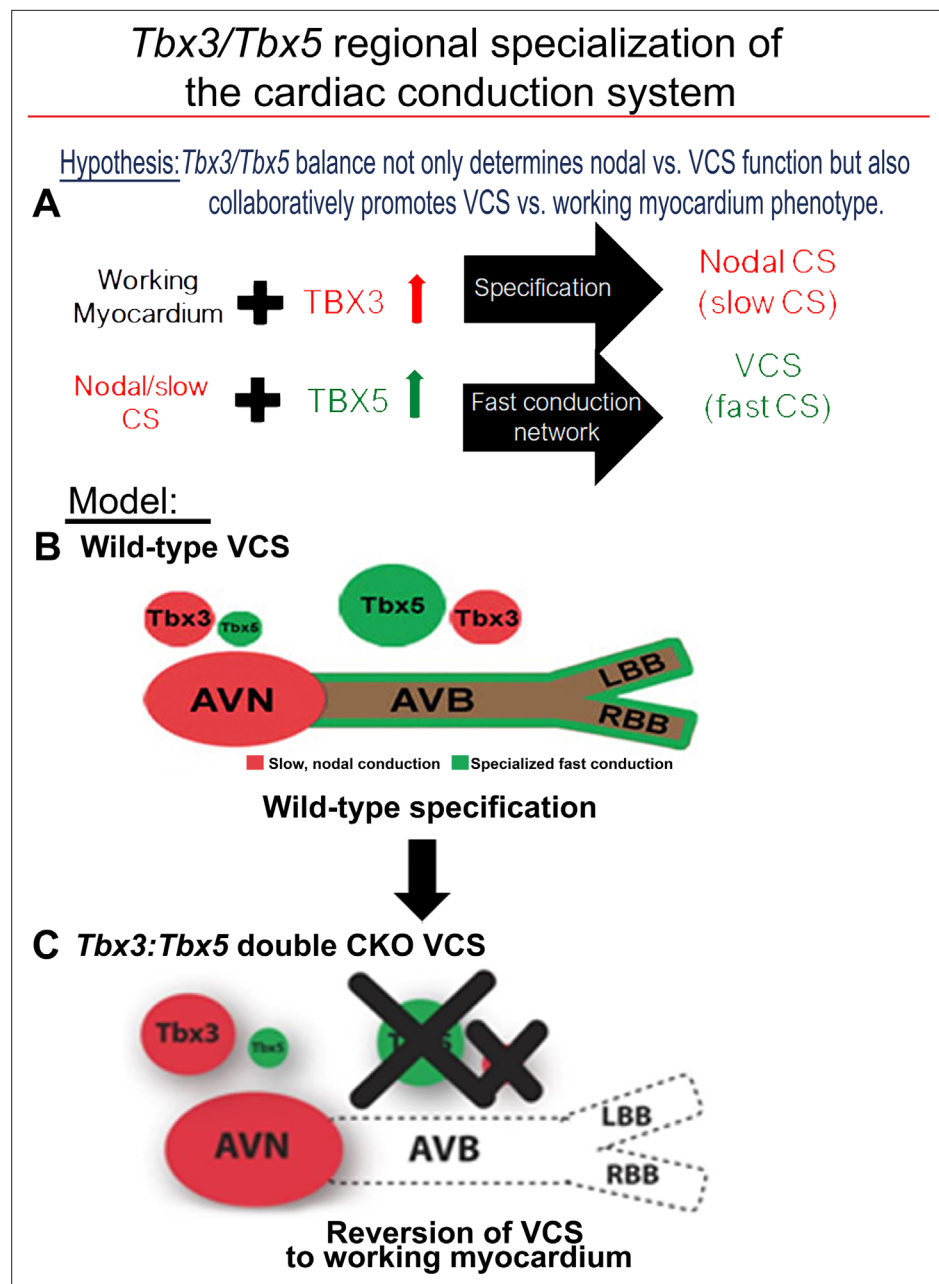


**Figure 7.** *Tbx3* and *Tbx5* play distinct roles in the adult VCS while collectively promoting CCS regional identity – a model elucidating our hypothesis for *Tbx3/Tbx5* dose-dependent CCS regional specialization. (A) The *Tbx3/Tbx5* balance not only governs nodal versus ventricular conduction system (VCS) function but also collaboratively promotes the VCS versus working myocardium (WM) phenotype. Specifically, a high level of *Tbx3* is linked to the specialization to the nodal conduction system, while an elevated *Tbx5* level in nodal cells activates local expression of the *Tbx5*-dependent fast conduction network, resulting in the generation of VCS. (B) CCS regional specialization is driven by local expression of *Tbx5*-dependent fast conduction network in the VCS, which overlaps underlying Pan-CCS expression of nodal, slow conduction network. (C) VCS-specific simultaneous genetic removal of both the *Tbx3* and *Tbx5* transcription factors transforms the fast-conducting, adult VCS into cells resembling working myocardium, thereby shifting them from conduction to non-conduction myocytes. Therefore, within the adult CCS, the *Tbx3* and *Tbx5* expression levels are crucial not only for normal fast versus slow conduction system identity but also for maintaining the conduction versus contraction specialization of the VCS. AVB, atrioventricular bundle; AVN, atrioventricular node; CCS, cardiac conduction system; CKO, conditional knockout; LBB, left bundle branch; RBB, right bundle branch; VCS, ventricular conduction system.

*Tbx5*-ablated VCS were due to retained expression of *Tbx3*. In fact, the autonomous beating and impulse initiation observed in the *Tbx5*-mutant VCS (Arnolds et al., 2012; Burnicka-Turek et al., 2020) were absent from the double *Tbx3:Tbx5* mutant VCS, further suggesting the transformation from a nodal-like to an inert myocardial functionally and a shift from conduction toward simple working myocardium.

Molecular studies support a transformation from conduction to working myocardium in the *Tbx3:Tbx5* double VCS knockout. Previous studies investigating the roles of *Tbx3* and *Tbx5* in maintaining adult VCS identity demonstrated that *Tbx3* deletion resulted in the silencing of Pan-CCS gene expression in the atrioventricular conduction system (van Duijvenboden et al., 2014; Bakker et al., 2012; Bruneau et al., 2001; Frank et al., 2011; Mohan et al., 2020). Alternately, specific deletion of *Tbx5* from the adult VCS led to the decreased expression of VCS-specific markers while Pan-CCS markers remained unchanged, indicating a transformation toward a nodal-like transcriptional phenotype in the absence of *Tbx5* (Arnolds et al., 2012; Burnicka-Turek et al., 2020). Consistently, a similar transformation was induced by *Tbx3* overexpression in the adult VCS. These findings underscored the significance of the *Tbx3:Tbx5* ratio in preserving the molecular and functional characteristics of the fast versus slow conduction system. In *Tbx3:Tbx5* double VCS knockout, we observed a reduction in the expression of both fast VCS markers and Pan-CCS markers transcribed throughout the entire CCS. As expected, not all VCS markers were ablated in VCS-specific *Tbx3:Tbx5* mutants. A significant portion of VCS fast conduction markers are also transcribed in ventricular working myocardium, albeit at lower levels than in the VCS, and are crucial for normal working myocardial function, for example, *Ryr2*, *Scn5a*, and *Kcnj2* (van Eif et al., 2020; Schram et al., 2002; Remme et al., 2009). Consistent with a shift from fast VCS to working myocardium, their expression levels are present, but at significantly lower levels in the double-knockout mutants than in normal VCS. Furthermore, the expression of markers specific for working myocardium, which are normally excluded in the VCS, emerged in the VCS of *Tbx3:Tbx5* double mutant. These observations are consistent with a transcriptional shift from VCS conduction cardiomyocytes to working myocardium-like characteristics in the absence of both *Tbx3* and *Tbx5*.

Our study highlights the critical role of *Tbx3* and *Tbx5* in maintaining the specialized electrical properties of the VCS. Comparative analysis of the phenotypes observed in single *Tbx3* or *Tbx5* knockouts and the *Tbx3:Tbx5* double-conditional knockout supports a coordinated function for these transcription factors in preserving VCS functionality. In a normal mammalian heart, electrical or optical recordings from the proximal part of the VCS typically display two distinct electrical excitations, reflected as two spikes in electrograms or two upstrokes in OAPs. These signals correspond to the sequential activation of the VCS, followed by ventricular excitation, a phenomenon well documented in both basic and clinical studies across species, including mice and humans. Previous whole-heart EP and optical mapping studies demonstrated that the single conditional knockout of *Tbx5* in the adult VCS caused significant ventricular conduction slowing (Arnolds et al., 2012), accompanied by a phenotypic shift of VCS cells toward a pacemaker-like cell, evidenced by ectopic beats originating in the ventricles, retrograde activation, and inappropriate automaticity (Burnicka-Turek et al., 2020). Whole-cell patch clamp recordings of *Tbx5*-deficient VCS cells further supported these findings, revealing action potential characteristics resembling pacemaker cells, including a slower upstroke (phase 0), prolonged plateau (phase 2), delayed repolarization (phase 3), and enhanced phase 4 depolarization (Burnicka-Turek et al., 2020). In contrast, reduced expression of *Tbx3* in the *Tbx3* haplo-insufficiency model resulted in AV bundle hypoplasia, PR interval shortening, and prolonged QRS duration (Mohan et al., 2020). Optical mapping in these mice showed delayed apical activation with multiple small breakthroughs separated by regions of delayed activation. This fragmented activation pattern suggests that the reduced *Tbx3* expression impaired the homogeneity and efficiency of ventricular electrical impulse propagation due to AV bundle and bundle branch hypoplasia (Mohan et al., 2020). In the *Tbx3:Tbx5* double-conditional knockout mice, we observed a complete loss of fast VCS conduction, similar to the phenotype of the *Tbx5* single conditional knockouts. However, unlike in the *Tbx5* single CKO, the VCS in *Tbx3:Tbx5* double mutants did not acquire pacemaker-like activity. Instead, optical mapping revealed a single upstroke in the His bundle region of *Tbx3:Tbx5* double-conditional knockout mice, indicating the absence of rapid AV bundle electrical impulse propagation. Functionally, this transformation resulted in significantly slowed ventricular activation, without the retrograde activation observed in the *Tbx5* single conditional knockouts or the rapid electrical

impulse propagation typically associated with an intact VCS. The homogenous morphological and molecular transformation of His bundle and VCS cells in the *Tbx3:Tbx5* double-conditional knockout mice rendered the electrical properties of the VCS-located cells functionally indistinguishable from those of ventricular working myocardium. Our data, including gene expression analysis of the double mutant VCS, are most consistent with the transition of double mutant VCS cells toward a working myocardium phenotype.

These findings emphasize the interdependent roles of *Tbx3* and *Tbx5* in maintaining the specialized electrical properties and identity of the VCS, distinguishing it from non-specialized ventricular working myocardium (**Figure 7**). While *Tbx5* alone is critical for suppressing pacemaker-like characteristics and preserving fast conduction properties, *Tbx3* plays a pivotal role in ensuring the structural and functional integrity of the AV and BB conduction pathways. The simultaneous deletion of both *Tbx3* and *Tbx5* disrupts these regulatory mechanisms, leading to a loss of VCS identity and a functional shift toward a working myocardium phenotype. Our study combined with prior literature (**Arnolds et al., 2012; van Duijvenboden et al., 2014; Burnicka-Turek et al., 2020; Bakker et al., 2012; Frank et al., 2011; Mohan et al., 2020; van Eif et al., 2018**) indicates that the concurrent presence of both *Tbx3* and *Tbx5* is necessary for maintaining VCS identity in the adult heart, ensuring efficient electrical conduction and preventing the transition of VCS cells into a working myocardium-like state (**Figure 7**).

## Methods

### Experimental animals

All animal experiments were performed under the University of Chicago Institutional Animal Care and Use Committee (IACUC) approved protocol (ACUP no. 71737) and in compliance with the USA Public Health Service Policy on Humane Care and Use of Laboratory Animals. *MinK<sup>CreERT2</sup>* [Tg(RP23-276l20-*MinKCreERT2*)] and *Tbx3<sup>fl/fl</sup>* mice have been reported previously (**Arnolds and Moskowitz, 2011b; Frank et al., 2011**).

*Tbx3:Tbx5* double-floxed mouse line was generated by University of Utah Core Research Facility using CRISPR/Cas9. Guide RNA (sgRNA) constructs were designed with software tools (ZiFiT Targeter **Sander et al., 2010** and [crispr.genome-engineering.org](http://crispr.genome-engineering.org)) predicting unique target sites throughout the mouse genome (**Figure 1—figure supplement 3–5**). The sgRNA constructs were transcribed in vitro using MEGAshortscript T7 (Invitrogen AM1354) and mMessage Machine T7 transcription kit (Invitrogen AM1344) according to the manufacturer's instructions. The strategy to generate mouse founders involved a single-step microinjection into one-cell *Tbx3* floxed zygotes (on a mixed background) with 10 ng/μl of each sgRNA (*Tbx5*-I2-S22 and *Tbx5*-I3-S31, **Figure 1—figure supplements 3–5**), 30 ng/μl of Cas9 protein, and 10 ng/μl of a long ssDNA donor. The donor contained two lox2272 sites in cis, spanning partial intron 2, entire exon 3, and partial intron 3 of the mouse *Tbx5* gene, along with 100/150 bp 5'/3' homology arms (**Figure 1—figure supplement 4**). Founders were validated by PCR, restriction enzyme digestion, and Sanger sequencing (**Figure 1—figure supplement 1B–D**). Founders were backcrossed with wild-type CD1 IGS mice (Charles River Lab, USA) to confirm germline transmission of the CRISPR/Cas9-generated compound *Tbx3:Tbx5* double-floxed allele and obtain the F1 generation. F1 mice were then interbred to establish a stable *Tbx3:Tbx5* double-floxed mouse line. Downstream experiments were performed on F4–F6 mice.

To simultaneously conditionally delete the *Tbx3* and *Tbx5* genes specifically from the adult VCS, we crossed our *Tbx3:Tbx5* double-floxed mouse line (*Tbx3<sup>fl/fl</sup>;Tbx5<sup>fl/fl</sup>*) with a VCS-specific tamoxifen (TM)-inducible Cre transgenic mouse line (*MinK<sup>CreERT2</sup>* [Tg(RP23-276l20-*MinKCreERT2*); **Arnolds and Moskowitz, 2011b; Figure 1A**]). All mice were maintained on a mixed genetic background. Tamoxifen (MP Biomedical) was administered at a dose of 0.167 mg/g body weight for 5 consecutive days by oral gavage at 6 weeks of age and then mice were evaluated at 9 weeks of age, as previously described (**Arnolds et al., 2012; Arnolds and Moskowitz, 2011b; Burnicka-Turek et al., 2020**). Age-, gender-, and genetic strain-matched controls were used in all experiments to account for any variations in datasets across experiments. Mice were bred and housed in specific pathogen-free conditions in a 12-hr light/12-hr dark cycle and allowed ad libitum access to standard mouse chow and water. Mice requiring medical attention were provided with appropriate veterinary care by a licensed veterinarian and were excluded from the experiments described. No other exclusion criteria were applied.

All experiments and subsequent analysis were conducted in a blinded fashion, with animals randomly assigned to experimental groups. Following genotyping, mice were randomly allocated to the studies based on their genotypes. Subsequently, their identities were anonymized using a numerical code to ensure that all experiments and analyses were performed in a blinded manner. Both male and female animals have been used in our studies in the ratio of 41%/59%, based on availability of relatively rare compound genotypes, respectively.

## Validation of the newly generated *Tbx5* floxed allele

The *Tbx3:Tbx5* double-floxed mouse line (*Tbx3<sup>fl/fl</sup>;Tbx5<sup>fl/fl</sup>*) was engineered by generating a novel *Tbx5* floxed allele in the background of a previously published *Tbx3* floxed allele (Frank et al., 2011). We utilized single *Tbx3* (Frank et al., 2011) and the novel *Tbx5* floxed mouse lines (*Tbx3<sup>fl/fl</sup>* and *Tbx5<sup>fl/fl</sup>*, respectively) to serve as controls in our studies (Figure 1A, Figure 1—figure supplements 1 and 2). Although the newly engineered *Tbx5* floxed allele was designed to mirror a previously published allele (Bruneau et al., 2001), the location of the flox sites was altered slightly, requiring validation.

To verify the ability of the newly generated *Tbx5* floxed allele to recombine into the *Tbx5* KO (null) allele, we conducted three rounds of breeding and utilized a PCR assay to distinguish the recombined *Tbx5* KO (null) allele (*Tbx5<sup>-</sup>*) from the unrecombined floxed allele (*Tbx5<sup>fl</sup>*) (Figure 1—figure supplement 2A, B). First, we bred newly generated homozygous *Tbx5* floxed males (*Tbx5<sup>fl/fl</sup>*) with homozygous *Mef2C<sup>Cre/Cre</sup>* females, which express Cre recombinase at the zygote stage (Hoffmann et al., 2014; Xie et al., 2012; Verzi et al., 2005), to produce germline *Tbx5<sup>+/-</sup>;Mef2C<sup>Cre/+</sup>* double heterozygous mice. PCR analysis showed that 100% of the generated offspring were *Tbx5<sup>+/-</sup>;Mef2C<sup>Cre/+</sup>* double heterozygous mice (Figure 1—figure supplement 2B). This result confirmed complete recombination of the new *Tbx5* floxed allele into the *Tbx5* null allele in the presence of the *Mef2C<sup>Cre</sup>* allele. Next, we backcrossed *Tbx5<sup>+/-</sup>;Mef2C<sup>Cre/+</sup>* double heterozygote mice with wild-type CD1 IGS mice (Charles River Lab, USA) to obtain a germline *Tbx5<sup>+/-</sup>* heterozygous mouse line (Figure 1—figure supplement 2B). Subsequently, we bred *Tbx5<sup>+/-</sup>* mice to generate germline *Tbx5* null mice (*Tbx5<sup>-/-</sup>*). Among 230 offspring (generated in 50 litters), we observed 113 wild-type pups (*Tbx5<sup>+/+</sup>*) and 116 *Tbx5* heterozygous pups (*Tbx5<sup>+/-</sup>*), but no null newborn pups (*Tbx5<sup>-/-</sup>*) were obtained (Figure 1—figure supplement 2B). These results align with previous breeding outcomes indicating complete embryonic lethality of *Tbx5* null mice (Bruneau et al., 2001).

To further confirm the ability of the newly generated *Tbx5* floxed allele to produce germline *Tbx5* null embryos (*Tbx5<sup>-/-</sup>*), we bred *Tbx5* heterozygous mice and collected embryos at E9–E10. Genotyping analysis of 89 collected embryos from 10 timed pregnancies revealed the presence of 24 wild-type (*Tbx5<sup>+/+</sup>*), 42 heterozygous (*Tbx5<sup>+/-</sup>*), and 22 null (*Tbx5<sup>-/-</sup>*) embryos (Figure 1—figure supplement 2C). Supported by Chi-square analysis, these results collectively verified that the newly generated *Tbx5* floxed allele could recombine to form the null allele, mimicking the embryonic lethality observed with the previously generated allele (Bruneau et al., 2001).

To confirm that the newly engineered *Tbx5* conditional allele can generate VCS-specific *Tbx5*-deficient mice with the same phenotype as VCS-specific *Tbx5* knockout mice obtained from the previously generated allele (Arnolds et al., 2012; Burnicka-Turek et al., 2020; Bruneau et al., 2001), we crossed the newly generated *Tbx5* floxed mouse line (*Tbx5<sup>fl/fl</sup>*) with a VCS-specific tamoxifen-inducible Cre transgenic mouse line (*Mink<sup>CreERT2</sup>* [Tg(RP23-276120-MinkCreERT2)]) (Arnolds and Moskowitz, 2011b; Figure 1A). The same tamoxifen regimen was administered as in the previous study (Arnolds et al., 2012; Burnicka-Turek et al., 2020). We confirmed VCS-specific genetic deletion of *Tbx5* via immunofluorescence (IF) (Figure 1B) and qPCR (Figure 1C). The resulting VCS-specific *Tbx5*-deficient mice exhibited slowed conduction, indicated by increased PR and QRS intervals (Figure 2A, and E vs. B), as well as episodes of VT resulting in sudden death (Figure 2G, H), consistent with the previously reported phenotype (Arnolds et al., 2012; Burnicka-Turek et al., 2020). Additionally, we confirmed the absence of histological and structural abnormalities in these mice, aligning with previous findings (Figure 3A, F vs. B, and K vs. G, respectively) (Arnolds et al., 2012; Burnicka-Turek et al., 2020).

## Echocardiography studies

Transthoracic echocardiography in mice was conducted under inhaled isoflurane anesthesia administered through a nose cone. Prior to imaging, chest hairs were removed using a topical depilatory agent. Limb leads were affixed for electrocardiogram gating, and animals were imaged in the left



lateral decubitus position with a VisualSonics Vevo 770 machine using a 30-MHz high-frequency transducer. To ensure stability, body temperature was carefully maintained using a heated imaging platform and warming lamps. Two-dimensional images were meticulously recorded in parasternal long- and short-axis projections, accompanied by guided M-mode recordings at the midventricular level in both views. LV cavity size and percent FS were measured in at least three beats from each projection and averaged. M-mode measurements were employed to ascertain LV chamber dimensions and percent LV FS, calculated as  $(\text{LVIDd} - \text{LVIDs})/\text{LVIDd}$ , where LVIDd and LVIDs represent LV internal diameter in diastole and systole, respectively.

## Surface ECG

Nine weeks old, tamoxifen-treated control and mutant mice were anesthetized with a mixture of 2–3% isoflurane in 100% oxygen. Anesthetized mice were secured in a supine position on a regulated heat pad while lead I and lead II ECGs were recorded using platinum subdermal needle electrodes in a three-limb configuration. Core temperature was continuously monitored using a rectal probe and maintained at 36–37°C throughout the procedure. ECG data were collected and analyzed using Ponemah Physiology Platform (DSI) software and an ACQ-7700 acquisition interface unit (Gould Instruments, Valley View, OH, USA). Key parameters derived from the ECG measurements included: heart rate (HR), PR interval (from the beginning of the P wave to the beginning of the QRS complex), and QRS complex duration.

## Telemetry ECG analysis

Nine weeks old, tamoxifen-treated control and mutant mice were anesthetized with 2–3% isoflurane in 100% oxygen, and wireless telemetry transmitters (ETA-F10; DSI) were surgically implanted in the back with leads tunneled to the right upper and left lower thorax, as previously described (**Arnolds et al., 2012; Wheeler et al., 2004**). Following a 24-hr recovery period after surgical instrumentation, heart rate and PR and QRS intervals were calculated using Ponemah Physiology Platform (DSI) from 48-hr recordings.

## Catheter-based intracardiac EP

Detailed protocols for invasive EP studies have been previously described (**Nadadur et al., 2016; Liu et al., 2008**). Briefly, 9 weeks old, tamoxifen-treated control and mutant mice were anesthetized using 2–3% isoflurane in 100% oxygen. Then, a 1.1-Fr octapolar electrode catheter (EPR-800; Millar Instruments) was advanced via a right jugular venous cut-down to record right atrial, His bundle, and RV potentials, as well as to perform programmed electrical stimulation. Signals were identified through alignment with simultaneous surface ECG using subcutaneous needle electrodes in a lead II configuration. ‘Near-Field’ and ‘Far-Field’ signals were identified based on ECG alignment, signal deflection upstroke speed, and total signal duration. Standard tachycardia induction protocols included an eight-beat drive train with beats 80–120 ms apart (S1), followed by five beats (S2) at 50 ms apart (penta-extrastimulus, PES). Two attempts at this PES protocol were carried out. Mice also underwent single extrastimulus testing (SES) with eight beats 80–120 ms apart (S1) followed by a single S2 at 50 ms. This SES protocol was carried out five separate times per mouse. If these two protocols in the right atrium and RV (separately) failed to initiate their respective tachycardias, the study was deemed negative. S1 drive train intervals varied slightly due to the presence of the AV Wenckebach block at faster pacing rates in some mice; the S1 interval was lengthened to prevent this during the drive train.

Additional atrial and ventricular pacing protocols were carried out to obtain atrial, atrio-ventricular, and ventricular effective refractory periods (AERP, AVERP, and VERP) as well as sinus node recovery time, as described previously (**Nadadur et al., 2016; Liu et al., 2008; Patel et al., 2003; Gehrman and Berul, 2000**). Effective refractory periods were measured using eight-beat S1 drive trains of 100 ms followed by SES.

## ECG and optical mapping

### ECG acquisition and analysis

ECGs were recorded in conscious *Tbx3:Tbx5* double-conditional knockout mice and control littermates using the ecgTUNNEL device (emka Technologies) 2 weeks after tamoxifen treatment. Mice were positioned in the tunnel and ECGs were recorded for 5 min at a sampling rate of 1 kHz using lead

I. ECGs were analyzed using a custom MATLAB program to measure P and QRS durations, as well as PR, QT, and RR intervals (George *et al.*, 2020; Warhol *et al.*, 2021; Figure 5—figure supplement 1).

## Langendorff perfusion

*Tbx3:Tbx5* double-conditional knockout mice ( $n = 8$ ) and control littermates ( $n = 10$ ) were deeply anesthetized with isoflurane. The heart was quickly excised following cervical dislocation and thoracotomy. The aorta was cannulated, and the heart was retrogradely perfused with warmed ( $37^{\circ}\text{C}$ ) and oxygenated (95%  $\text{O}_2$  and 5%  $\text{CO}_2$ ) modified Tyrode's solution (in mM, NaCl 130,  $\text{NaHCO}_3$  24,  $\text{NaH}_2\text{PO}_4$  1.2,  $\text{MgCl}_2$  1, glucose 5.6, KCl 4, and  $\text{CaCl}_2$  1.8) at a pH of 7.4. The heart was placed in a constant-flow (1.0–2.0 ml/min) Langendorff perfusion system, laying horizontally in a tissue bath.

## Ventricular optical mapping

The Langendorff perfused heart was electromechanically uncoupled by 15  $\mu\text{M}$  of blebbistatin (Cayman Chemicals 13186) perfusion. A voltage-sensitive fluorescent dye, 80  $\mu\text{M}$  di-4-ANEPPs (Thermo Fisher Scientific D1199), was administered through the dye injection port. The heart was illuminated using a  $520 \pm 5$  nm (Prizmatix, UHP-Mic-LED-520) wavelength light source to excite di-4-ANEPPs. Emitted photons were captured using complementary metal–oxide semiconductor cameras (MiCAM, SciMedia).

The stimulation threshold, where the heart would capture the stimuli and action potential 1:1, was determined using a point source platinum electrode placed on the anterior surface of the heart on the anterior epicardial surface of the ventricles. Pacing was applied at 1.5 $\times$  the threshold amplitude to maintain 1:1 capture over the duration of the experiment. Optical recordings were analyzed using Rhythm 1.2 to analyze transmembrane potential (Cathey *et al.*, 2019). Action potential duration at 50% and 80% repolarization was calculated for the ventricles of the intact whole heart preparation.

## Right septal preparation optical mapping experiments

Following intact whole heart ex vivo optical mapping, the heart was removed from the tissue bath for the dissection of the RV free wall to expose the RV septal surface (Tamaddon *et al.*, 2000). The heart was quickly returned to the tissue bath and the RV septal surface was focused into the field of view. Sinus rhythm optical recordings were acquired.

A custom MATLAB program was written to plot individual pixels in a  $100 \times 100$  pixel image stack. A Butterworth filter of order 5 was applied to provide temporal filtering (Laughner *et al.*, 2012). The location of the His bundle was identified as the region at the base of the interventricular septum (a red  $10 \times 10$  pixel area in Figure 5B). Signals from the working ventricular myocardium were recorded from the  $10 \times 10$  pixel region plotted in the working ventricular myocardium distal to the His bundle (Figure 6B).

## Isolation of adult VCS cardiomyocytes and cell sorting

Adult mouse EYFP-positive VCS cardiomyocytes were isolated using the method described by Mitra and Morad, 1985. Briefly, 9 weeks old tamoxifen-treated control and *Tbx3:Tbx5* double-conditional mutant mice were heparinized (100 units IP) and anesthetized with pentobarbital (50 mg/kg of body weight). Hearts were excised and mounted on a Langendorff apparatus, then perfused with  $\text{Ca}^{2+}$ -free Tyrode's solution with collagenase B and D (Roche Chemical Co) plus protease (Fraction IV, Sigma Chemical Co). When the hearts appeared pale and flaccid, they were removed from the Langendorff apparatus and a tip of ventricular septum below the AV annulus was microdissected out (Arnolds *et al.*, 2012; Park and Fishman, 2011; Silverman *et al.*, 2006) and kept in  $\text{Ca}^{2+}$ -free Tyrode's solution with 1 mg/ml of bovine serum albumin (Fraction XIV, Sigma Chemical Co). The intraventricular sections were then minced into small pieces  $\sim 1 \times 1 \times 1$  mm and then gently triturated with a Pasteur pipette to dissociate individual VCS myocytes. Propidium iodide (Thermo Fisher Scientific) was added immediately before FACS to facilitate live/dead discrimination. Cells were sorted on a FACS Aria flow cytometer (BD Biosciences) located at the University of Chicago Flow Cytometry Core using Influx software. Samples from wild-type age-matched hearts were used for gating. Samples were gated to exclude debris and cell clumps. Fluorescent cells were collected into ice-cold RNase-free PBS and processed for RNA extraction and protein isolation.

## RNA isolation and qRT-PCR

Total RNA was isolated from EYFP-positive VCS cardiomyocytes sorted from 9-week-old control and VCS-specific *Tbx3:Tbx5*-deficient mice, which had received tamoxifen at 6 weeks of age. RNA was also extracted from atrial and ventricular tissues dissected from the same mice. All RNA extractions were performed using RNeasy Mini Kit (QIAGEN), followed by DNase treatment according to the manufacturer's instructions.

Reverse transcription reaction was carried out using the SuperScript III First-Strand Synthesis SuperMix for quantitative RT-PCR (Invitrogen) as per the manufacturer's recommendations. qRT-PCR was performed using the POWER SYBR Green PCR master mix from Applied Biosystems and run on an Applied Biosystems AB7500 machine in 96-well plates. The relative gene expression level was calculated by the  $\Delta\Delta C_t$  method (Livak and Schmittgen, 2001) using glyceraldehyde-3-phosphate dehydrogenase (*Gapdh*) gene expression level as internal control. The data presented are the average of three independent experiments.

## Protein isolation and western blotting

Total protein was isolated from EYFP-positive VCS cardiomyocytes sorted from 9-week-old control and VCS-specific *Tbx3:Tbx5*-deficient mice that had been administered tamoxifen at 6 weeks of age. Protein was also obtained from atrial and ventricular tissues dissected from the same animals. The tissues were snap-frozen in liquid nitrogen, pulverized, and homogenized in RIPA buffer (50 mM Tris-HCl pH 8, 150 mM NaCl, 1% Triton-X, 0.5% sodium deoxycholate, 0.1% SDS, 5 mM EDTA) with 1 Roche EDTA-Free complete protease inhibitor tablet per 50 ml of buffer. Samples were tumbled for 1 hr at 4°C and then centrifuged for 10 min at 13,200  $\times$  g. Protein concentration was determined using the BCA assay (Pierce) with BSA as a standard.

For Western blot analysis, 25  $\mu$ g of protein was diluted in Laemmli buffer, heated at 70°C for 10 min, and subjected to SDS-PAGE on 4–20% TGX gels (Bio-Rad). Proteins were then transferred to nitrocellulose membranes, blocked with 5% milk in TBS-T, and incubated overnight at 4°C with primary antibodies diluted in 2.5% milk in TBS-T. The primary antibodies used were: goat polyclonal anti-TBX3 (Santa Cruz Biotechnology, sc-31656, 1:250), rabbit polyclonal anti-HCN4 (Millipore, AB5808, 1:500), rabbit polyclonal anti-CAV1.3/CACNA1D (Alomone, ACC-005, 1:200), rabbit polyclonal anti-Cx45/GJC1 (Thermo Fisher Scientific, PA5-77357, 1:250), sheep polyclonal anti-TBX5 (R&D, AF5918, 1:200), rabbit polyclonal anti-CX40/GJA5 (Zymed/Invitrogen, 36-4900, 1:500), rabbit polyclonal anti-NAV1.5/SCN5A (Alomone, ASC-005, 1:200), mouse monoclonal anti-KCNK3/TASK1 (Abcam, ab186352, 1:1000), rabbit polyclonal anti-CX43/GJA1 (Cell Signaling Technology, 3512, 1:1000), and mouse monoclonal anti-GAPDH (Abcam, ab8245, 1:1000). After rinsing in TBS-T, membranes were incubated for 1 hr at room temperature (RT) with secondary antibodies diluted in 2.5% milk in TBS-T, rinsed again, and visualized using enhanced chemiluminescence reagents (Pierce ECL/ECL Plus, Thermo Fisher Scientific) and Kodak X-OMAT film. Results were normalized to GAPDH loading control and then quantified using ImageJ software (Rasband, 1997; Wheeler et al., 2004). Secondary antibodies used were donkey anti-goat IgG AlexaFluor-594 (Invitrogen, A-11058, 1:250 dilution) and donkey anti-goat IgG AlexaFluor-488 (Invitrogen, A-11055, 1:250 dilution) for experiments involving co-staining for goat primary antibodies. Secondary antibodies were as follows: rabbit anti-goat-HRP (Jackson ImmunoResearch, 305-035-003, 1:10,000), goat anti-rabbit-HRP (Jackson ImmunoResearch, 111-035-144, 1:3000), donkey anti-sheep-HRP (Abcam, ab6900, 1:5000), and sheep anti-mouse-HRP (Amersham GE, NA931, 1:2500).

## Histology

Hearts from 9-week-old control and mutant mice were carefully dissected, flushed with ice-cold PBS, and then fixed for 48 hr at 4°C in a 4% paraformaldehyde solution (Sigma-Aldrich). Following fixation, the hearts were processed for paraffin-embedded sections and subjected to analysis through H&E staining, following the manufacturer's protocol provided by Sigma-Aldrich.

## Immunofluorescence

Hearts from 9-week-old control and mutant mice were dissected out and placed in ice-cold PBS, followed by freezing in OCT (Fisher) within the gas phase of liquid nitrogen. Cryosections of 7  $\mu$ m thickness were mounted onto Superfrost Plus glass slides (Fisher Scientific), air-dried, and fixed for

10 min in ice-cold 4% paraformaldehyde (Sigma-Aldrich). Subsequently, sections were permeabilized in 1% Triton-X100 (Sigma-Aldrich) in PBS for 10 min, then blocked in 10% normal goat serum (Invitrogen) in PBS-T (PBS + 0.1% Tween-20) for 30 min at RT. Sections were then incubated overnight at 4°C in primary antibody diluted in blocking buffer, rinsed in PBS, then subsequently incubated for 60 min at RT in secondary antibody diluted in blocking buffer. Slides were mounted in VectaShield + DAPI (Vector Laboratories) or counterstained with DAPI and mounted in ProLog Gold (Invitrogen) prior to visualizing fluorescence. Primary antibodies were as follows: goat polyclonal anti-TBX3 (Santa Cruz, sc-31656, 1:250 dilution) and goat polyclonal anti-TBX5 (Santa Cruz, sc-17866, 1:250 dilution). Secondary antibodies used were donkey anti-goat IgG AlexaFluor-594 (Invitrogen, A-11058, 1:250 dilution) and donkey anti-goat IgG AlexaFluor-488 (Invitrogen, A-11055, 1:250 dilution) for experiments involving co-staining for goat primary antibodies. A secondary antibody-only control was employed in each case to ensure the specificity of immunostaining.

Statistics

The numbers of independent experiments are specified in the relevant figure legends. Quantitative data are presented as mean ± SD. Statistical analysis was performed using R version 3.6.2 or the GraphPad Prism statistical package version 10.2.1 (GraphPad Software, Boston, MA, USA). For all datasets, except qRT-PCR data, normality was assessed using the Shapiro–Wilk normality test. If the data followed a normal distribution, the two-sample Welch *t*-test was performed for comparison. If normal distribution was not present, the non-parametric Mann–Whitney *U* test or Kruskal–Wallis *H* test was used, as indicated in the text. Statistical significance was assumed if *p* reached a value ≤0.05. For qRT-PCR data, statistical analysis was performed using R version 4.2.0. Normality within each experimental group was assessed using the Shapiro–Wilk test. Between-group comparisons were conducted using Welch *t*-test, and multiple comparisons were corrected using the Benjamini and Hochberg method to control the false discovery rate (FDR) (Benjamini and Hochberg, 1995). If a significant difference was detected between two groups (*t*-test FDR <0.05) but normality was rejected in any of the compared groups (Shapiro–Wilk *p* < 0.05), a non-parametric Wilcoxon rank-sum test was used for verification. A significant group-mean difference was confirmed at one-tailed Wilcoxon *p* ≤ 0.05 (Source data 1).

Acknowledgements

This work was supported by National Institutes of Health (R01 HL163523 and R01 HL148719 to IP Moskowitz), Leducq Foundation Grant Bioelectronics for Neuroradiology – Diagnosis & Therapeutics (to IR Efimov), and American Heart Association (13POST17290028 to O Burnicka-Turek).

Additional information

Funding

Funder	Grant reference number	Author
National Institutes of Health	R01 HL163523	Ivan P Moskowitz
National Institutes of Health	R01 HL148719	Ivan P Moskowitz
Leducq Foundation Grant Bioelectronics for Neuroradiology – Diagnosis & Therapeutics		Igor R Efimov
American Heart Association	13POST17290028	Ozanna Burnicka-Turek
The funders had no role in study design, data collection, and interpretation, or the decision to submit the work for publication.		




### Author contributions

Ozanna Burnicka-Turek, Conceptualization, Data curation, Formal analysis, Supervision, Validation, Investigation, Visualization, Methodology, Writing – original draft, Project administration, Writing – review and editing; Katy A Trampel, Conceptualization, Data curation, Formal analysis, Validation, Investigation, Visualization, Methodology, Writing – original draft, Writing – review and editing; Brigitte Laforest, Data curation, Formal analysis, Validation, Investigation, Visualization; Michael T Broman, Resources, Data curation, Formal analysis, Supervision, Validation, Investigation, Visualization, Methodology; Xinan H Yang, Data curation, Formal analysis, Visualization, Writing – review and editing; Zoheb Khan, Margaret Gadek, Kaitlyn M Shen, Data curation, Validation, Investigation; Eric Rytkin, Binjie Li, Investigation, Methodology; Ella Schaffer, Data curation, Investigation, Visualization; Igor R Efimov, Conceptualization, Resources, Formal analysis, Supervision, Funding acquisition, Methodology, Writing – original draft, Project administration, Writing – review and editing; Ivan P Moskowitz, Conceptualization, Resources, Supervision, Funding acquisition, Writing – original draft, Project administration, Writing – review and editing


### Author ORCIDs

Ozanna Burnicka-Turek  <https://orcid.org/0000-0002-3770-4314>

Katy A Trampel  <https://orcid.org/0000-0001-5735-1037>

Brigitte Laforest  <https://orcid.org/0000-0001-6919-8922>

Igor R Efimov  <https://orcid.org/0000-0002-1483-5039>

Ivan P Moskowitz  <https://orcid.org/0000-0003-0014-4963>

### Ethics

All animal experiments were performed under the University of Chicago Institutional Animal Care and Use Committee (IACUC) approved protocol (ACUP no. 71737) and in compliance with the USA Public Health Service Policy on Humane Care and Use of Laboratory Animals.

### Peer review material

Reviewer #2 (Public review): <https://doi.org/10.7554/eLife.102027.3.sa1>

Reviewer #3 (Public review): <https://doi.org/10.7554/eLife.102027.3.sa2>

Author response <https://doi.org/10.7554/eLife.102027.3.sa3>

---

## Additional files

### Supplementary files

Source data 1. Expanded statistical analysis of the qRT-PCR data presented in **Figures 1C, 3L and 4A–C**. Statistical analyses were performed in R (v4.2.0). Normality for each experimental group was assessed using the Shapiro-Wilk test. Group comparisons were conducted using Welch's t-test, with multiple testing correction by the Benjamini & Hochberg method to control the false discovery rate (FDR) (74). If  $FDR < 0.05$  but normality was rejected (Shapiro-Wilk  $P < 0.05$ ), significance was confirmed using a one-tailed Wilcoxon rank-sum test ( $P \leq 0.05$ ).

MDAR checklist

### Data availability

All data generated and analyzed during this study are included in the main manuscript and its supplementary materials. The source data for statistical analyses are provided in Source Data 1. Uncropped gels and blots have been supplied for Figure 1-figure supplements 1 and 2, as well as for Figure 4. No additional data are required to interpret the findings.

## References

- Ackerman JE, Muscat SN, Adjei-Sowah E, Korcari A, Nichols AEC, Buckley MR, Loisel AE. 2024. Identification of Periostin as a critical niche for myofibroblast dynamics and fibrosis during tendon healing. *Matrix Biology* **125**:59–72. DOI: <https://doi.org/10.1016/j.matbio.2023.12.004>, PMID: 38101460
- Alcoléa S, Théveniau-Ruissy M, Jarry-Guichard T, Marics I, Tzouanacou E, Chauvin JP, Briand JP, Moorman AF, Lamers WH, Gros DB. 1999. Downregulation of connexin 45 gene products during mouse heart development. *Circulation Research* **84**:1365–1379. DOI: <https://doi.org/10.1161/01.res.84.12.1365>, PMID: 10381888

- Arnolds DE**, Chu A, McNally EM, Nobrega MA, Moskowitz IP. 2011a. The emerging genetic landscape underlying cardiac conduction system function. *Birth Defects Research. Part A, Clinical and Molecular Teratology* **91**:578–585. DOI: <https://doi.org/10.1002/bdra.20800>, PMID: 21538814
- Arnolds DE**, Moskowitz IP. 2011b. Inducible recombination in the cardiac conduction system of minK: CreERT. *Genesis* **49**:878–884. DOI: <https://doi.org/10.1002/dvg.20759>, PMID: 21504046
- Arnolds DE**, Liu F, Fahrenbach JP, Kim GH, Schillinger KJ, Smemo S, McNally EM, Nobrega MA, Patel VV, Moskowitz IP. 2012. TBX5 drives Scn5a expression to regulate cardiac conduction system function. *The Journal of Clinical Investigation* **122**:2509–2518. DOI: <https://doi.org/10.1172/JCI62617>
- Bakker ML**, Boukens BJ, Mommersteeg MTM, Brons JF, Wakker V, Moorman AFM, Christoffels VM. 2008. Transcription factor Tbx3 is required for the specification of the atrioventricular conduction system. *Circulation Research* **102**:1340–1349. DOI: <https://doi.org/10.1161/CIRCRESAHA.107.169565>, PMID: 18467625
- Bakker ML**, Boink GJJ, Boukens BJ, Verkerk AO, van den Boogaard M, den Haan AD, Hoogaars WMH, Buermans HP, de Bakker JMT, Seppen J, Tan HL, Moorman AFM, 't Hoen PAC, Christoffels VM. 2012. T-box transcription factor TBX3 reprogrammes mature cardiac myocytes into pacemaker-like cells. *Cardiovascular Research* **94**:439–449. DOI: <https://doi.org/10.1093/cvr/cvs120>
- Bamshad M**, Lin RC, Law DJ, Watkins WC, Krakowiak PA, Moore ME, Franceschini P, Lala R, Holmes LB, Gebuhr TC, Bruneau BG, Schinzel A, Seidman JG, Seidman CE, Jorde LB. 1997. Mutations in human TBX3 alter limb, apocrine and genital development in ulnar-mammary syndrome. *Nature Genetics* **16**:311–315. DOI: <https://doi.org/10.1038/ng0797-311>
- Basson CT**, Cowley GS, Solomon SD, Weissman B, Poznanski AK, Traill TA, Seidman JG, Seidman CE. 1994. The clinical and genetic spectrum of the Holt-Oram syndrome (heart-hand syndrome). *The New England Journal of Medicine* **330**:885–891. DOI: <https://doi.org/10.1056/NEJM199403313301302>, PMID: 8114858
- Basson CT**, Bachinsky DR, Lin RC, Levi T, Elkins JA, Soultis J, Grayzel D, Kroumpouzou E, Traill TA, Leblanc-Straceski J, Renault B, Kucherlapati R, Seidman JG, Seidman CE. 1997. Mutations in human TBX5 [corrected] cause limb and cardiac malformation in Holt-Oram syndrome. *Nature Genetics* **15**:30–35. DOI: <https://doi.org/10.1038/ng0197-30>, PMID: 8988165
- Benjamini Y**, Hochberg Y. 1995. Controlling the false discovery rate: a practical and powerful approach to multiple testing. *Journal of the Royal Statistical Society Series B* **57**:289–300. DOI: <https://doi.org/10.1111/j.2517-6161.1995.tb02031.x>
- Bruneau BG**, Nemer G, Schmitt JP, Charron F, Robitaille L, Caron S, Conner DA, Gessler M, Nemer M, Seidman CE, Seidman JG. 2001. A murine model of Holt-Oram syndrome defines roles of the T-box transcription factor Tbx5 in cardiogenesis and disease. *Cell* **106**:709–721. DOI: [https://doi.org/10.1016/s0092-8674\(01\)00493-7](https://doi.org/10.1016/s0092-8674(01)00493-7), PMID: 11572777
- Burnicka-Turek O**, Broman MT, Steimle JD, Boukens BJ, Petrenko NB, Ikegami K, Nadadur RD, Qiao Y, Arnolds DE, Yang XH, Patel VV, Nobrega MA, Efimov IR, Moskowitz IP. 2020. Transcriptional patterning of the ventricular cardiac conduction system. *Circulation Research* **127**:e94–e106. DOI: <https://doi.org/10.1161/CIRCRESAHA.118.314460>, PMID: 32290757
- Cathey B**, Obaid S, Zolotarev AM, Pryamonoosov RA, Syunyaev RA, George SA, Efimov IR. 2019. Open-Source Multiparametric Optocardiography. *Scientific Reports* **9**:721. DOI: <https://doi.org/10.1038/s41598-018-36809-y>, PMID: 30679527
- Donner BC**, Schullenberg M, Geduldig N, Hüning A, Mersmann J, Zacharowski K, Kovacevic A, Decking U, Aller MI, Schmidt KG. 2011. Functional role of TASK-1 in the heart: studies in TASK-1-deficient mice show prolonged cardiac repolarization and reduced heart rate variability. *Basic Research in Cardiology* **106**:75–87. DOI: <https://doi.org/10.1007/s00395-010-0128-x>
- Dow LE**, Fisher J, O'Rourke KP, Muley A, Kastnerhuber ER, Livshits G, Tschaharganeh DF, Socci ND, Lowe SW. 2015. Inducible in vivo genome editing with CRISPR-Cas9. *Nature Biotechnology* **33**:390–394. DOI: <https://doi.org/10.1038/nbt.3155>, PMID: 25690852
- Frank DU**, Carter KL, Thomas KR, Burr RM, Bakker ML, Coetzee WA, Tristani-Firouzi M, Bamshad MJ, Christoffels VM, Moon AM. 2011. Lethal arrhythmias in Tbx3-deficient mice reveal extreme dosage sensitivity of cardiac conduction system function and homeostasis. *PNAS* **109**:154–163. DOI: <https://doi.org/10.1073/pnas.1115165109>
- Garcia-Frigola C**, Shi Y, Evans SM. 2003. Expression of the hyperpolarization-activated cyclic nucleotide-gated cation channel HCN4 during mouse heart development. *Gene Expression Patterns* **3**:777–783. DOI: [https://doi.org/10.1016/s1567-133x\(03\)00125-x](https://doi.org/10.1016/s1567-133x(03)00125-x), PMID: 14643687
- Gehrmann J**, Berul CI. 2000. Cardiac electrophysiology in genetically engineered mice. *Journal of Cardiovascular Electrophysiology* **11**:354–368. DOI: <https://doi.org/10.1111/j.1540-8167.2000.tb01806.x>, PMID: 10749360
- George SA**, Kiss A, Obaid SN, Venegas A, Talapatra T, Wei C, Efimova T, Efimov IR. 2020. p38δ genetic ablation protects female mice from anthracycline cardiotoxicity. *American Journal of Physiology. Heart and Circulatory Physiology* **319**:H775–H786. DOI: <https://doi.org/10.1152/ajpheart.00415.2020>, PMID: 32822209
- Graham V**, Zhang H, Willis S, Creazzo TL. 2006. Expression of a two-pore domain K<sup>+</sup> channel (TASK-1) in developing avian and mouse ventricular conduction systems. *Developmental Dynamics* **235**:143–151. DOI: <https://doi.org/10.1002/dvdy.20558>
- Greener ID**, Monfredi O, Inada S, Chandler NJ, Tellez JO, Atkinson A, Taube M-A, Billeter R, Anderson RH, Efimov IR, Molenaar P, Sigg DC, Sharma V, Boyett MR, Dobrzynski H. 2011. Molecular architecture of the human specialised atrioventricular conduction axis. *Journal of Molecular and Cellular Cardiology* **50**:642–651. DOI: <https://doi.org/10.1016/j.yjmcc.2010.12.017>, PMID: 21256850

- Gurumurthy CB**, O'Brien AR, Quadros RM, Adams J Jr, Alcaide P, Ayabe S, Ballard J, Batra SK, Beauchamp M-C, Becker KA, Bernas G, Brough D, Carrillo-Salinas F, Chan W, Chen H, Dawson R, DeMambro V, D'Hont J, Dibb K, Eudy JD, et al. 2021. Response to correspondence on "Reproducibility of CRISPR-Cas9 methods for generation of conditional mouse alleles: a multi-center evaluation". *Genome Biology* **22**:99. DOI: <https://doi.org/10.1186/s13059-021-02320-3>, PMID: 33827648
- Hatcher CJ**, Basson CT. 2009. Specification of the cardiac conduction system by transcription factors. *Circulation Research* **105**:620–630. DOI: <https://doi.org/10.1161/CIRCRESAHA.109.204123>, PMID: 19797194
- Hiroi Y**, Kudoh S, Monzen K, Ikeda Y, Yazaki Y, Nagai R, Komuro I. 2001. Tbx5 associates with Nkx2-5 and synergistically promotes cardiomyocyte differentiation. *Nature Genetics* **28**:276–280. DOI: <https://doi.org/10.1038/90123>, PMID: 11431700
- Hoffmann AD**, Yang XH, Burnicka-Turek O, Bosman JD, Ren X, Steimle JD, Vokes SA, McMahon AP, Kalinichenko VV, Moskowitz IP. 2014. Foxf genes integrate tbx5 and hedgehog pathways in the second heart field for cardiac septation. *PLOS Genetics* **10**:e1004604. DOI: <https://doi.org/10.1371/journal.pgen.1004604>, PMID: 25356765
- Hoogaars WM**, Tessari A, Moorman AF, Boer PA, Hagoort J, Soufan AT, Campione M, Christoffels VM. 2004. The transcriptional repressor Tbx3 delineates the developing central conduction system of the heart. *Cardiovascular Research* **62**:489–499. DOI: <https://doi.org/10.1016/j.cardiores.2004.01.030>
- Hoogaars WMH**, Barnett P, Moorman AFM, Christoffels VM. 2007a. T-box factors determine cardiac design. *Cellular and Molecular Life Sciences* **64**:646–660. DOI: <https://doi.org/10.1007/s00018-007-6518-z>, PMID: 17380306
- Hoogaars WMH**, Engel A, Brons JF, Verkerk AO, de Lange FJ, Wong LYE, Bakker ML, Clout DE, Wakker V, Barnett P, Ravensloot JH, Moorman AFM, Verheijck EE, Christoffels VM. 2007b. Tbx3 controls the sinoatrial node gene program and imposes pacemaker function on the atria. *Genes & Development* **21**:1098–1112. DOI: <https://doi.org/10.1101/gad.416007>, PMID: 17473172
- Hua X**, Wang Y-Y, Jia P, Xiong Q, Hu Y, Chang Y, Lai S, Xu Y, Zhao Z, Song J. 2020. Multi-level transcriptome sequencing identifies COL1A1 as a candidate marker in human heart failure progression. *BMC Medicine* **18**:2. DOI: <https://doi.org/10.1186/s12916-019-1469-4>, PMID: 31902369
- Huikuri HV**, Castellanos A, Myerburg RJ. 2001. Sudden death due to cardiac arrhythmias. *The New England Journal of Medicine* **345**:1473–1482. DOI: <https://doi.org/10.1056/NEJMr000650>, PMID: 11794197
- Kempen MJA**, Vermeulen JLM, Moorman AFM, Gros DB, Paul DL, Lamers WH. 1996. Developmental changes of connexin40 and connexin43 mRNA distribution patterns in the rat heart. *Cardiovascular Research* **32**:886–900. DOI: [https://doi.org/10.1016/0008-6363\(96\)00131-9](https://doi.org/10.1016/0008-6363(96)00131-9)
- Laughner JI**, Ng FS, Sulkin MS, Arthur RM, Efimov IR. 2012. Processing and analysis of cardiac optical mapping data obtained with potentiometric dyes. *American Journal of Physiology. Heart and Circulatory Physiology* **303**:H753–H765. DOI: <https://doi.org/10.1152/ajpheart.00404.2012>, PMID: 22821993
- Li QY**, Newbury-Ecob RA, Terrett JA, Wilson DI, Curtis AR, Yi CH, Gebuhr T, Bullen PJ, Robson SC, Strachan T, Bonnet D, Lyonnet S, Young ID, Raeburn JA, Buckler AJ, Law DJ, Brook JD. 1997. Holt-Oram syndrome is caused by mutations in TBX5, a member of the Brachyury (T) gene family. *Nature Genetics* **15**:21–29. DOI: <https://doi.org/10.1038/ng0197-21>, PMID: 8988164
- Liang X**, Wang G, Lin L, Lowe J, Zhang Q, Bu L, Chen Y, Chen J, Sun Y, Evans SM. 2013. HCN4 dynamically marks the first heart field and conduction system precursors. *Circulation Research* **113**:399–407. DOI: <https://doi.org/10.1161/CIRCRESAHA.113.301588>, PMID: 23743334
- Linden H**, Williams R, King J, Blair E, Kini U. 2009. Ulnar Mammary syndrome and TBX3: expanding the phenotype. *American Journal of Medical Genetics* **149A**:2809–2812. DOI: <https://doi.org/10.1002/ajmg.a.33096>
- Liu F**, Levin MD, Petrenko NB, Lu MM, Wang T, Yuan LJ, Stout AL, Epstein JA, Patel VV. 2008. Histone-deacetylase inhibition reverses atrial arrhythmia inducibility and fibrosis in cardiac hypertrophy independent of angiotensin. *Journal of Molecular and Cellular Cardiology* **45**:715–723. DOI: <https://doi.org/10.1016/j.yjmcc.2008.08.015>, PMID: 18926829
- Livak KJ**, Schmittgen TD. 2001. Analysis of relative gene expression data using real-time quantitative PCR and the 2(-Delta Delta C(T)) Method. *Methods* **25**:402–408. DOI: <https://doi.org/10.1006/meth.2001.1262>, PMID: 11846609
- Mangoni ME**, Traboulsie A, Leoni A-L, Couette B, Marger L, Le Quang K, Kupfer E, Cohen-Solal A, Vilar J, Shin H-S, Escande D, Charpentier F, Nargeot J, Lory P. 2006. Bradycardia and slowing of the atrioventricular conduction in mice lacking CaV3.1/alpha1G T-type calcium channels. *Circulation Research* **98**:1422–1430. DOI: <https://doi.org/10.1161/01.RES.0000225862.14314.49>, PMID: 16690884
- Marionneau C**, Couette B, Liu J, Li H, Mangoni ME, Nargeot J, Lei M, Escande D, Demolombe S. 2005. Specific pattern of ionic channel gene expression associated with pacemaker activity in the mouse heart. *The Journal of Physiology* **562**:223–234. DOI: <https://doi.org/10.1113/jphysiol.2004.074047>, PMID: 15498808
- Meneghini V**, Odent S, Platonova N, Egeo A, Merlo GR. 2006. Novel TBX3 mutation data in families with ulnar-mammary syndrome indicate a genotype-phenotype relationship: Mutations that do not disrupt the T-domain are associated with less severe limb defects. *European Journal of Medical Genetics* **49**:151–158. DOI: <https://doi.org/10.1016/j.ejmg.2005.04.021>
- Miquerol L**, Moreno-Rascon N, Beyer S, Dupays L, Meilhac SM, Buckingham ME, Franco D, Kelly RG. 2010. Biphasic development of the mammalian ventricular conduction system. *Circulation Research* **107**:153–161. DOI: <https://doi.org/10.1161/CIRCRESAHA.110.218156>, PMID: 20466980

- Mitra R**, Morad M. 1985. A uniform enzymatic method for dissociation of myocytes from hearts and stomachs of vertebrates. *The American Journal of Physiology* **249**:H1056–H1060. DOI: <https://doi.org/10.1152/ajpheart.1985.249.5.H1056>, PMID: 2998207
- Mohan RA**, Bosada FM, van Weerd JH, van Duijvenboden K, Wang J, Mommersteeg MTM, Hooijkaas IB, Wakker V, de Gier-de Vries C, Coronel R, Boink GJJ, Bakkers J, Barnett P, Boukens BJ, Christoffels VM. 2020. T-box transcription factor 3 governs a transcriptional program for the function of the mouse atrioventricular conduction system. *PNAS* **117**:18617–18626. DOI: <https://doi.org/10.1073/pnas.1919379117>, PMID: 32675240
- Mori AD**, Zhu Y, Vahora I, Nieman B, Koshiba-Takeuchi K, Davidson L, Pizard A, Seidman JG, Seidman CE, Chen XJ, Henkelman RM, Bruneau BG. 2006. Tbx5-dependent rheostatic control of cardiac gene expression and morphogenesis. *Developmental Biology* **297**:566–586. DOI: <https://doi.org/10.1016/j.ydbio.2006.05.023>, PMID: 16870172
- Moskowitz IPG**, Pizard A, Patel VV, Bruneau BG, Kim JB, Kupersmidt S, Roden D, Berul CI, Seidman CE, Seidman JG. 2004. The T-Box transcription factor Tbx5 is required for the patterning and maturation of the murine cardiac conduction system. *Development* **131**:4107–4116. DOI: <https://doi.org/10.1242/dev.01265>, PMID: 15289437
- Moskowitz IPG**, Kim JB, Moore ML, Wolf CM, Peterson MA, Shendure J, Nobrega MA, Yokota Y, Berul C, Izumo S, Seidman JG, Seidman CE. 2007. A molecular pathway including Id2, Tbx5, and Nkx2-5 required for cardiac conduction system development. *Cell* **129**:1365–1376. DOI: <https://doi.org/10.1016/j.cell.2007.04.036>, PMID: 17604724
- Munshi NV**. 2012. Gene regulatory networks in cardiac conduction system development. *Circulation Research* **110**:1525–1537. DOI: <https://doi.org/10.1161/CIRCRESAHA.111.260026>, PMID: 22628576
- Nadadur RD**, Broman MT, Boukens B, Mazurek SR, Yang X, van den Boogaard M, Bekeny J, Gadek M, Ward T, Zhang M, Qiao Y, Martin JF, Seidman CE, Seidman J, Christoffels V, Efimov IR, McNally EM, Weber CR, Moskowitz IP. 2016. Pitx2 modulates a Tbx5-dependent gene regulatory network to maintain atrial rhythm. *Science Translational Medicine* **8**:354ra115. DOI: <https://doi.org/10.1126/scitranslmed.aaf4891>, PMID: 27582060
- Oka T**, Xu J, Kaiser RA, Melendez J, Hambleton M, Sargent MA, Lorts A, Brunskill EW, Dorn GW, Conway SJ, Aronow BJ, Robbins J, Molkentin JD. 2007. Genetic manipulation of periostin expression reveals a role in cardiac hypertrophy and ventricular remodeling. *Circulation Research* **101**:313–321. DOI: <https://doi.org/10.1161/CIRCRESAHA.107.149047>, PMID: 17569887
- Pan X**, Chen X, Ren Q, Yue L, Niu S, Li Z, Zhu R, Chen X, Jia Z, Zhen R, Ban J, Chen S. 2022. Single-cell transcriptomics identifies Col1a1 and Col1a2 as hub genes in obesity-induced cardiac fibrosis. *Biochemical and Biophysical Research Communications* **618**:30–37. DOI: <https://doi.org/10.1016/j.bbrc.2022.06.018>, PMID: 35714568
- Park DS**, Fishman GI. 2011. The cardiac conduction system. *Circulation* **123**:904–915. DOI: <https://doi.org/10.1161/CIRCULATIONAHA.110.942284>, PMID: 21357845
- Patel VV**, Arad M, Moskowitz IPG, Maguire CT, Branco D, Seidman JG, Seidman CE, Berul CI. 2003. Electrophysiologic characterization and postnatal development of ventricular pre-excitation in a mouse model of cardiac hypertrophy and Wolff-Parkinson-White syndrome. *Journal of the American College of Cardiology* **42**:942–951. DOI: [https://doi.org/10.1016/s0735-1097\(03\)00850-7](https://doi.org/10.1016/s0735-1097(03)00850-7), PMID: 12957447
- Rasband WS**. 1997. ImageJ, u. s. national institutes of health, Bethesda, MD, USA, 1997-2016. 0.1. ImageJ. <http://imagej.nih.gov/ij>
- Remme CA**, Verkerk AO, Hoogaars WMH, Aanhaenen WTJ, Scicluna BP, Annink C, van den Hoff MJB, Wilde AAM, van Veen TAB, Veldkamp MW, de Bakker JMT, Christoffels VM, Bezzina CR. 2009. The cardiac sodium channel displays differential distribution in the conduction system and transmural heterogeneity in the murine ventricular myocardium. *Basic Research in Cardiology* **104**:511–522. DOI: <https://doi.org/10.1007/s00395-009-0012-8>, PMID: 19255801
- Rubart M**, Zipes DP. 2005. Mechanisms of sudden cardiac death. *The Journal of Clinical Investigation* **115**:2305–2315. DOI: <https://doi.org/10.1172/JCI26381>, PMID: 16138184
- Sander JD**, Maeder ML, Reyon D, Voytas DF, Joung JK, Dobbs D. 2010. ZiFIT (Zinc Finger Targeter): an updated zinc finger engineering tool. *Nucleic Acids Research* **38**:W462–W468. DOI: <https://doi.org/10.1093/nar/gkq319>, PMID: 20435679
- Scheinman MM**. 2009. Role of the His-Purkinje system in the genesis of cardiac arrhythmia. *Heart Rhythm* **6**:1050–1058. DOI: <https://doi.org/10.1016/j.hrthm.2009.03.011>
- Schram G**, Pourrier M, Melnyk P, Nattel S. 2002. Differential distribution of cardiac ion channel expression as a basis for regional specialization in electrical function. *Circulation Research* **90**:939–950. DOI: <https://doi.org/10.1161/01.res.0000018627.89528.6f>
- Silverman ME**, Grove D, Upshaw CB. 2006. Why does the heart beat? The discovery of the electrical system of the heart. *Circulation* **113**:2775–2781. DOI: <https://doi.org/10.1161/CIRCULATIONAHA.106.616771>, PMID: 16769927
- Tamaddon HS**, Vaidya D, Simon AM, Paul DL, Jalife J, Morley GE. 2000. High-resolution optical mapping of the right bundle branch in connexin40 knockout mice reveals slow conduction in the specialized conduction system. *Circulation Research* **87**:929–936. DOI: <https://doi.org/10.1161/01.res.87.10.929>, PMID: 11073890
- van den Boogaard M**, Wong LY, Tessadori F, Bakker ML, Dreizehnter LK, Wakker V, Bezzina CR, 't Hoen PAC, Bakkers J, Barnett P, Christoffels VM. 2012. Genetic variation in T-box binding element functionally affects SCN5A/SCN10A enhancer. *Journal of Clinical Investigation* **122**:2519–2530. DOI: <https://doi.org/10.1172/JCI62613>



- van Duijvenboden K, Ruijter JM, Christoffels VM. 2014. Gene regulatory elements of the cardiac conduction system. *Briefings in Functional Genomics* **13**:28–38. DOI: <https://doi.org/10.1093/bfpg/elt031>, PMID: 23969024
- van Eif VWW, Devalla HD, Boink GJJ, Christoffels VM. 2018. Transcriptional regulation of the cardiac conduction system. *Nature Reviews. Cardiology* **15**:617–630. DOI: <https://doi.org/10.1038/s41569-018-0031-y>, PMID: 29875439
- van Eif VWW, Stefanovic S, Mohan RA, Christoffels VM. 2020. Gradual differentiation and confinement of the cardiac conduction system as indicated by marker gene expression. *Biochimica et Biophysica Acta. Molecular Cell Research* **1867**:118509. DOI: <https://doi.org/10.1016/j.bbamcr.2019.07.004>, PMID: 31306714
- van Weerd JH, Christoffels VM. 2016. The formation and function of the cardiac conduction system. *Development* **143**:197–210. DOI: <https://doi.org/10.1242/dev.124883>, PMID: 26786210
- Verheule S, Kaese S. 2013. Connexin diversity in the heart: insights from transgenic mouse models. *Frontiers in Pharmacology* **4**:81. DOI: <https://doi.org/10.3389/fphar.2013.00081>, PMID: 23818881
- Verzi MP, McCulley DJ, De Val S, Dodou E, Black BL. 2005. The right ventricle, outflow tract, and ventricular septum comprise a restricted expression domain within the secondary/anterior heart field. *Developmental Biology* **287**:134–145. DOI: <https://doi.org/10.1016/j.ydbio.2005.08.041>, PMID: 16188249
- Warhol A, George SA, Obaid SN, Efimova T, Efimov IR. 2021. Differential cardiotoxic electrocardiographic response to doxorubicin treatment in conscious versus anesthetized mice. *Physiological Reports* **9**:e14987. DOI: <https://doi.org/10.14814/phy2.14987>, PMID: 34337891
- Wheeler MT, Allikian MJ, Heydemann A, Hadhazy M, Zarnegar S, McNally EM. 2004. Smooth muscle cell-extrinsic vascular spasm arises from cardiomyocyte degeneration in sarcoglycan-deficient cardiomyopathy. *The Journal of Clinical Investigation* **113**:668–675. DOI: <https://doi.org/10.1172/JCI20410>, PMID: 14991064
- Wu S, Liu M, Zhang M, Ye X, Gu H, Jiang C, Zhu H, Ye X, Li Q, Huang X, Cao M. 2024. The gene expression of CALD1, CDH2, and POSTN in fibroblast are related to idiopathic pulmonary fibrosis. *Frontiers in Immunology* **15**:1275064. DOI: <https://doi.org/10.3389/fimmu.2024.1275064>
- Xie L, Hoffmann AD, Burnicka-Turek O, Friedland-Little JM, Zhang K, Moskowitz IP. 2012. Tbx5-hedgehog molecular networks are essential in the second heart field for atrial septation. *Developmental Cell* **23**:280–291. DOI: <https://doi.org/10.1016/j.devcel.2012.06.006>, PMID: 22898775
- Zhao J, Lv T, Quan J, Zhao W, Song J, Li Z, Lei H, Huang W, Ran L. 2018. Identification of target genes in cardiomyopathy with fibrosis and cardiac remodeling. *Journal of Biomedical Science* **25**:63. DOI: <https://doi.org/10.1186/s12929-018-0459-8>, PMID: 30115125

# Appendix 1

## Appendix 1—key resources table

Reagent type (species) or resource	Designation	Source or reference	Identifiers	Additional information
Antibody	Goat polyclonal anti-TBX3	Santa Cruz Biotechnology	sc-31656	IF (1:250) WB (1:250)
Antibody	Goat polyclonal anti-TBX5	Santa Cruz Biotechnology	sc-17866	IF (1:250)
Antibody	Donkey anti-goat IgG AlexaFluor-594	Invitrogen	A-11058	IF (1:250)
Antibody	Donkey anti-goat IgG AlexaFluor-488	Invitrogen	A-11055	IF (1:250)
Antibody	Rabbit polyclonal anti-HCN4	Millipore	AB5808	WB (1:500)
Antibody	Rabbit polyclonal anti-CAV1.3/CACNA1D	Alomone	ACC-005	WB (1:200)
Antibody	Rabbit polyclonal anti-Cx45/GJC1	Thermo Fisher	PA5-77357	WB (1:250)
Antibody	Sheep polyclonal anti-TBX5	R&D	AF5918	WB (1:200)
Antibody	Rabbit polyclonal anti-CX40/GJA5	Zymed/ Invitrogen	36-4900	WB (1:500)
Antibody	Rabbit polyclonal anti-NAV1.5/SCN5A	Alomone	ASC-005	WB (1:200)
Antibody	Mouse monoclonal anti-KCNK3/TASK1	Abcam	ab186352	WB (1:1000)
Antibody	Rabbit polyclonal anti-CX43/GJA1	Cell Signalling Technology	3512	WB (1:1000)
Antibody	Mouse monoclonal anti-GAPDH	Abcam	ab8245	WB (1:1000)
Antibody	Rabbit anti-goat-HRP	Jackson Immuno Research	305-035-003	WB (1:10 000)
Antibody	Goat anti-rabbit-HRP	Jackson Immuno Research	111-035-144	WB (1:3000)
Antibody	Donkey anti-sheep-HRP	Abcam	ab6900	WB (1:5000)
Antibody	Sheep anti-mouse-HRP	Amersham GE	NA931	WB (1:2500)
Chemical compound, drug	BSA	Sigma-Aldrich	A9576	
Chemical compound, drug	cOmplete, Mini, EDTA-free Protease Inhibitor Cocktail	Roche	11836170001	
Chemical compound, drug	DAPI	Invitrogen	62248	
Chemical compound, drug	Isoflurane	Sigma-Aldrich	26675-46-7	
Chemical compound, drug	POWER SYBR Green PCR Master Mix	Applied Biosystems	43-676-59	
Chemical compound, drug	ProLong Gold Antifade Mountant	Invitrogen	P10144	
Chemical compound, drug	Propidium Iodide	Thermo Fisher Scientific	P3566	
Chemical compound, drug	Tamoxifen	MP Biomedical		Dosage details look at Materials & Methods section
Commercial assay or kit	MEGAscript T7 transcription kit	Invitrogen	AM1354	
Commercial assay or kit	mMessage Machine T7 transcription kit	Invitrogen	AM1344	

Appendix 1 Continued on next page

## Appendix 1 Continued

Reagent type (species) or resource	Designation	Source or reference	Identifiers	Additional information
Commercial assay or kit	Pierce BCA Protein Assay Kit	Thermo Fisher Scientific	23225	
Commercial assay or kit	Pierce ECL	Thermo Fisher Scientific	32106	
Commercial assay or kit	Pierce ECL Plus	Thermo Fisher Scientific	32132	
Commercial assay or kit	RNeasy Mini Kit	Qiagen	74104	
Commercial assay or kit	SuperScript III First-Strand Synthesis SuperMix	Invitrogen	18080400	
Genetic reagent ( <i>M. musculus</i> )	Tbx3 <sup>fl/fl</sup> ;Tbx5 <sup>fl/fl</sup> Mixed 129/SvJ:C57BL/6 J:CD-1 background	This paper		Generated using CRISPR–Cas9 technology (look at Experimental animals section)
Genetic reagent ( <i>M. musculus</i> )	Tbx3 <sup>fl/fl</sup> ;Tbx5 <sup>fl/fl</sup> ; R26R <sup>eYFP/+</sup> ; MinK <sup>CreERT2/+</sup> Mixed 129/SvJ:C57BL/6 J:CD-1 background	This paper		Generated using CRISPR–Cas9 technology (look at Experimental animals section)
Genetic reagent ( <i>M. musculus</i> )	Kcne1 <sup>CreERT2</sup> [Tg(RP23-276I20-MinKCreERT2)] – referred to as MinK <sup>CreERT2</sup> in the manuscript for consistency with field-standard nomenclature and to avoid confusion. Mixed 129/SvJ:C57BL/6 J:CD-1 background	PMID: 21504046		Dr. Ivan P. Moskowitz (University of Chicago)
Genetic reagent ( <i>M. musculus</i> )	Tbx3 <sup>fl/fl</sup> Mixed 129/SvJ:C57BL/6 J:CD-1 background	PMID: 22203979		Dr. Anne M Moon (University of Utah)
Genetic reagent ( <i>M. musculus</i> )	CD-1	Charles Rivers Laboratories		<a href="https://www.criver.com/products-services/find-model/cd-1r-igs-mouse?region=3611">https://www.criver.com/products-services/find-model/cd-1r-igs-mouse?region=3611</a>
Genetic reagent ( <i>M. musculus</i> )	C57BL/6 J	Jackson Laboratory		<a href="https://www.jax.org/strain/000664">https://www.jax.org/strain/000664</a>
Other	Long ssDNA donor	This paper		Sequence details look at <b>Figure 1—figure supplement 4</b>
Other	SDS-PAGE on 4–20% TGX Gels	Bio-Rad	4561096	4–20% Mini-PROTEAN TGX Precast Protein Gels
Other	Tbx5-I2-S22	This paper	sgRNA	Sequence details look at <b>Figure 1—figure supplement 3</b>
Other	Tbx5-I2-S31	This paper	sgRNA	Sequence details look at <b>Figure 1—figure supplement 3</b>
Other	VectaShield +DAPI	Vector Laboratories		<a href="https://vectorlabs.com/vectashield-mounting-medium-with-dapi.html">https://vectorlabs.com/vectashield-mounting-medium-with-dapi.html</a>
Sequence-based reagent	Tbx5 locus: 5'arm-F	This paper	PCR primers	Sequence details look at <b>Figure 1—figure supplement 5</b>
Sequence-based reagent	Tbx5 locus: 5'arm-R	This paper	PCR primers	Sequence details look at <b>Figure 1—figure supplement 5</b>
Sequence-based reagent	Tbx5 locus: 3'arm-F	This paper	PCR primers	Sequence details look at <b>Figure 1—figure supplement 5</b>
Sequence-based reagent	Tbx5 locus: 3'arm-R	This paper	PCR primers	Sequence details look at <b>Figure 1—figure supplement 5</b>
Sequence-based reagent	Tbx3 locus: WT-F	PMID: 22203979	PCR primers	Dr. Anne M Moon (University of Utah)

Appendix 1 Continued on next page

Appendix 1 Continued

Reagent type (species) or resource	Designation	Source or reference	Identifiers	Additional information
Sequence-based reagent	Tbx3 locus: WT-R	PMID: 22203979	PCR primers	Dr. Anne M Moon (University of Utah)
Sequence-based reagent	Tbx3 locus: Flox-F	PMID: 22203979	PCR primers	Dr. Anne M Moon (University of Utah)
Sequence-based reagent	Tbx3 locus: Flox-R	PMID: 22203979	PCR primers	Dr. Anne M Moon (University of Utah)
Sequence-based reagent	qPCR_Tbx3-F	PMID: 32290757	qRT-PCR primers	5'-AGATCCGGTT ATCCCTGG GAC-3'
Sequence-based reagent	qPCR_Tbx3-R	PMID: 32290757	qRT-PCR primers	5'-CAGCAGCCCC CACTAAGT-3'
Sequence-based reagent	qPCR_Tbx5-F	PMID: 32290757	qRT-PCR primers	5'-GGCATGGAAG GAATCAAG GT-3'
Sequence-based reagent	qPCR_Tbx5-R	PMID: 32290757	qRT-PCR primers	5'-CTAGGAAACATT CTCCTCCC TGC-3'
Sequence-based reagent	qPCR_Gja1-F	PMID: 22086960 (Primer Bank ID:166091435 c3)	qRT-PCR primers	5'-ACAGCGGTTG AGTCAGCT TG-3'
Sequence-based reagent	qPCR_Gja1-R	PMID: 22086960 (Primer Bank ID:166091435 c3)	qRT-PCR primers	5'-GAGAGATGGG GAAGGACT TGT-3'
Sequence-based reagent	qPCR_Gja5-F	PMID: 32290757	qRT-PCR primers	5'-AGCTCCAGTC ACCCATCT TG-3'
Sequence-based reagent	qPCR_Gja5-R	PMID: 32290757	qRT-PCR primers	5'-CAGTTGAACA GCAGCCAG AG-3'
Sequence-based reagent	qPCR_Gjc1-F	PMID: 32290757	qRT-PCR primers	5'-AGATCCACAA CCATTCGA CATT-3'
Sequence-based reagent	qPCR_Gjc1-R	PMID: 32290757	qRT-PCR primers	5'-TCCCAGGTAC ATCACAGA GGG-3'
Sequence-based reagent	qPCR_Gjd3-F	PMID: 22086960 (Primer Bank ID: 30519904 a1)	qRT-PCR primers	5'-TCATGCTGAT CTTCCGCA TCC-3'
Sequence-based reagent	qPCR_Gjd3-R	PMID: 22086960 (Primer Bank ID: 30519904 a1)	qRT-PCR primers	5'-GAAGCGGTAG TGGGACACC-3'
Sequence-based reagent	qPCR_Scn5a-F	PMID: 32290757	qRT-PCR primers	5'-CGCTCCTCCA GGTAGATG TC-3'
Sequence-based reagent	qPCR_Scn5a-R	PMID: 32290757	qRT-PCR primers	5'-CTACCGCATA GTGGAGCA CA-3'
Sequence-based reagent	qPCR_Ryr2-F	PMID: 32290757	qRT-PCR primers	5'-CAAATCCTTC TGCTGCCA AG-3'
Sequence-based reagent	qPCR_Ryr2-R	PMID: 32290757	qRT-PCR primers	5'-CGAGGATGAG ATCCAGTT CC-3'
Sequence-based reagent	qPCR_Kcnk3-F	PMID: 32290757	qRT-PCR primers	5'-CTCCTTCTAC TTCGCCAT CA-3'
Sequence-based reagent	qPCR_Kcnk3-R	PMID: 32290757	qRT-PCR primers	5'-GAAGGTGTTG ATGCGTTCA-3'
Sequence-based reagent	qPCR_Kcnj2-F	PMID: 32290757	qRT-PCR primers	5'-CGACTGCCAT GACAACTC AA-3'
Sequence-based reagent	qPCR_Kcnj2-R	PMID: 32290757	qRT-PCR primers	5'-CATATCTCCG ATTCTCGCT-3'
Sequence-based reagent	qPCR_Kcnj3-F	PMID: 32290757	qRT-PCR primers	5'-GCTGGCAACT ACACTCCC TG-3'

Appendix 1 Continued on next page



Appendix 1 Continued

Reagent type (species) or resource	Designation	Source or reference	Identifiers	Additional information
Sequence-based reagent	qPCR_Kcnj3-R	PMID: 32290757	qRT-PCR primers	5'-AACATGCAGC CGATGAGG AA-3'
Sequence-based reagent	qPCR_Kcnj4-F	PMID: 32290757	qRT-PCR primers	5'-CACGTAAACG GCTTTTGGG-3'
Sequence-based reagent	qPCR_Kcnj4-R	PMID: 32290757	qRT-PCR primers	5'-CCGTCTCGAA CGGAGATG AC-3'
Sequence-based reagent	qPCR_Kcnj12-F	PMID: 32290757	qRT-PCR primers	5'-ACCCCTACAG CATCGTAT CAT-3'
Sequence-based reagent	qPCR_Kcnj12-R	PMID: 32290757	qRT-PCR primers	5'-GTTGCACTGA CCGTTCTT CTT-3'
Sequence-based reagent	qPCR_Hcn1-F	PMID: 22086960 (Primer Bank ID: 6754168 a1)	qRT-PCR primers	5'-CAAATTCCTCC CTCCGCAT GTT-3'
Sequence-based reagent	qPCR_Hcn1-R	PMID: 22086960 (Primer Bank ID: 6754168 a1)	qRT-PCR primers	5'-TGAAGAACGT GATTCCAA CTGG-3'
Sequence-based reagent	qPCR_Hcn4-F	PMID: 32290757	qRT-PCR primers	5'-GGCGGACACC GCTATCAA-3'
Sequence-based reagent	qPCR_Hcn4-R	PMID: 32290757	qRT-PCR primers	5'-TGCCGAACAT CCTTAGGG AGA-3'
Sequence-based reagent	qPCR_Cacna1d-F	PMID: 22086960 (Primer Bank ID: 27413155 a1)	qRT-PCR primers	5'-GACTGATGCC CGATATAA AGGC-3'
Sequence-based reagent	qPCR_Cacna1d-R	PMID: 22086960 (Primer Bank ID: 27413155 a1)	qRT-PCR primers	5'-CCTTCACCAGA AATAGGGA GTCT-3'
Sequence-based reagent	qPCR_Cacna1g-F	PMID: 32290757	qRT-PCR primers	5'-TGTCTCCGCA CGGTCTGT AA-3'
Sequence-based reagent	qPCR_Cacna1g-R	PMID: 32290757	qRT-PCR primers	5'-AGATACCCAA AGCGACCA TCTT-3'
Sequence-based reagent	qPCR_Cacna1h-F	PMID: 32290757	qRT-PCR primers	5'-GAACGTGGTT CTTTACAA CGGC-3'
Sequence-based reagent	qPCR_Cacna1h-R	PMID: 32290757	qRT-PCR primers	5'-GCACATAGTT CCCAAAGG TCA-3'
Sequence-based reagent	qPCR_Smpx-F	PMID: 22086960 (Primer Bank ID: 14149752 a1)	qRT-PCR primers	5'-ATGTCGAAGC AGCCAATT TCC-3'
Sequence-based reagent	qPCR_Smpx-R	PMID: 22086960 (Primer Bank ID: 14149752 a1)	qRT-PCR primers	5'-TCAGACAAGT TGACAACA GGTC-3'
Sequence-based reagent	qPCR_Col1a1-F	PMID: 22086960 (Primer Bank ID: 34328108 a1)	qRT-PCR primers	5'-GCTCCTCTTA GGGGCCACT-3'
Sequence-based reagent	qPCR_Col1a1-R	PMID: 22086960 (Primer Bank ID: 34328108 a1)	qRT-PCR primers	5'-CCACGTCTCA CCATTGGGG-3'
Sequence-based reagent	qPCR_Postn-F	PMID: 22086960 (Primer Bank ID: 7657429 a1)	qRT-PCR primers	5'-CCTGCCCTTA TATGCTCT GCT-3'
Sequence-based reagent	qPCR_Postn-R	PMID: 22086960 (Primer Bank ID: 7657429 a1)	qRT-PCR primers	5'-AAACATGGTCA ATAGGCAT CACT-3'